

ALMA Spectral Survey of An eruptive Young star, V883 Ori (ASSAY): II. Freshly Sublimated Complex Organic Molecules (COMs) in the Keplerian Disk

JAE-HONG JEONG,¹ JEONG-EUN LEE,^{1,2} SEONJAE LEE,¹ GISEON BAEK,^{1,3} JI-HYUN KANG,⁴ SEOKHO LEE,⁴ CHUL-HWAN KIM,¹ HYEONG-SIK YUN,⁴ YURI AIKAWA,⁵ GREGORY J. HERCZEG,^{6,7} DOUG JOHNSTONE,^{8,9} AND LUCAS CIEZA¹⁰

¹*Department of Physics and Astronomy, Seoul National University, 1 Gwanak-ro, Gwanak-gu, Seoul 08826, Korea*

²*SNU Astronomy Research Center, Seoul National University, 1 Gwanak-ro, Gwanak-gu, Seoul 08826, Republic of Korea*

³*Research Institute of Basic Sciences, Seoul National University, Seoul 08826, Republic of Korea*

⁴*Korea Astronomy and Space Science Institute, 776 Daedeok-daero, Yuseong, Daejeon 34055, Korea*

⁵*Department of Astronomy, University of Tokyo, 7-3-1 Hongo, Bunkyo-ku, Tokyo 113-0033, Japan*

⁶*Kavli Institute for Astronomy and Astrophysics, Peking University, Yiheyuan 5, Haidian Qu, 100871 Beijing, China*

⁷*Department of Astronomy, Peking University, Yiheyuan 5, Haidian Qu, 100871 Beijing, China*

⁸*NRC Herzberg Astronomy and Astrophysics, 5071 West Saanich Road, Victoria, BC, V9E 2E7, Canada*

⁹*Department of Physics and Astronomy, University of Victoria, 3800 Finnerty Road, Elliot Building, Victoria, BC, V8P 5C2, Canada*

¹⁰*Facultad de Ingeniería y Ciencias, Instituto de Estudios Astrofísicos, Universidad Diego Portales, Av. Ejercito 441. Santiago, Chile*

ABSTRACT

We present an investigation of Complex Organic Molecules (COMs) in the spatially resolved Keplerian disk around V883 Ori, an eruptive young star, based on a spectral survey carried out with ALMA in Band 6 (220.7–274.9 GHz). We identified about 3,700 molecular emission lines and discovered 23 COMs in the disk. We estimated the column densities of COMs detected through the iterative LTE line fitting method. According to our analyses, using only optically thin lines is critical to deriving the reliable column densities of COMs. Therefore, covering a large frequency range is important for the studies of COMs. The most distinct phenomenon found from the spectra of the V883 Ori disk is that nitrogen-bearing COMs other than CH₃CN are missing, whereas various oxygen-bearing COMs, except for the CH₂OH-bearing molecules, are detected. The missing CH₂OH-bearing COMs may indicate the warm water-ice dominant environment for forming COMs. We compared our results with various objects in different evolutionary stages, from Class 0 hot corinos to a Solar System comet 67P/Churyumov-Gerasimenko, to examine the effect of evolution on the COM compositions. In general, the COMs abundances relative to methanol in V883 Ori are higher than in the hot corinos and hot cores, while they are comparable to the cometary values. This may indicate the planet-forming material chemically evolves in the disk midplane after being accreted from the envelope. In addition, as found in the comet 67P/Churyumov-Gerasimenko, nitrogen might also be trapped as ammonium salt within the dust grains in the V883 Ori disk.

1. INTRODUCTION

Complex organic molecules (COMs) are prebiotic molecules with six or more atoms (Herbst & van Dishoeck 2009). COMs can be detected via their emission lines when they are desorbed to the gas phase from icy mantles of dust grains. They have been detected in various protostellar evolutionary stages and environments across various star-forming regions: prestellar

core (Öberg et al. 2010; Scibelli & Shirley 2020), hot corino (Jørgensen et al. 2016; Belloche et al. 2020; Yang et al. 2021; Hsu et al. 2022; Lee et al. 2023), hot core (Belloche et al. 2016; Baek et al. 2022; Chen et al. 2023), disk atmosphere (Lee et al. 2017, 2019a), disk midplane (van 't Hoff et al. 2018b; Lee et al. 2019b; Yamato et al. 2024), and an extended shell around protostellar clusters (McGuire et al. 2016).

However, it remains elusive as to the degree that COM compositions would change from the initial compositions of the prestellar stage as the protostar evolves, as well as which chemistry (grain-surface versus gas-phase) would be dominant for COMs at different evolutionary stages.

To answer these questions, we need to investigate COMs throughout the evolutionary stages. Although observational and theoretical studies have been done in various interstellar conditions to date (Ceccarelli et al. 2023), the study of COMs associated with disks is difficult (Aikawa et al. 2022; McGuire 2022).

It is because the sublimation regions of COMs in the disks of typical low-mass protostellar systems, especially at disk midplanes, are confined to a few au of radii due to the disk temperature profile and density structure. Thus, even the Atacama Large Millimeter Array (ALMA) cannot resolve the COM sublimation regions in most disks with central protostars in the quiescent accretion phase.

Accretion outbursts can be used to study COMs compositions in a disk because the sublimation radii of COMs expand to large radii due to the luminosity increase by the outburst, and thus, freshly sublimated COMs emission can be detected (e.g., van 't Hoff et al. (2018b); Lee et al. (2019b); Yamato et al. (2024); Lee et al. (2024)). From this idea, they could detect COMs emissions, revealing ice composition in the Keplerian disk of V883 Ori, including its midplane. However, these previous studies covered only narrow spectral ranges, limiting the full investigation of chemical characteristics in the V883 Ori disk.

An unbiased spectral line survey allows us to more fully understand a source's chemical properties. Excellent examples for ALMA spectral survey projects include Exploring Molecular Complexity with ALMA (EMoCA) for hot cores of Sgr B2(N) (Belloche et al. 2016) and Protostellar Interferometric Line Survey (PILS) for a hot corino IRAS 16293-2422 (Jørgensen et al. 2016). These results have significantly contributed to our understanding of hot core and hot corino chemistry by discovering various new COMs from the unbiased continuous coverage of thousands of molecular lines (Jørgensen et al. 2020).

As an extension of these surveys, we carried out an unbiased spectral survey of V883 Ori to explore the disk chemical composition more thoroughly within the limit of observational sensitivity. V883 Ori is an eruptive young stellar object in transition between Class I and Class II, located within the Orion Molecular Cloud at a distance of 388 pc (Lee et al. 2019b). The bolometric luminosity of V883 Ori is still controversial, ranging from 186 L_{\odot} (Furlan et al. 2016) to 285 L_{\odot} (Strom & Strom 1993; Sandell & Weintraub 2001) when they are adjusted to the distance of 388 pc. The outburst, which began before 1888, has lasted more than 130 years and may have been more luminous at its peak. (Strom & Strom 1993). Its disk inclination is 38.3° , and the mass

of the protostar is $1.2 M_{\odot}$ (Cieza et al. 2016; Lee et al. 2019b). Our spectral survey on V883 Ori fully covers 220.7 to 274.9 GHz using ALMA Band 6 with a uniform sensitivity rather than targeting specific species.

In this paper, we report the results of our COMs analyses with the V883 Ori spectral survey data, focusing on oxygen- and nitrogen-bearing species. In Section 2, we describe our spectral survey observation and extraction of the spectra for the spectral analyses. In Section 3, we explain the method of line identification as well as how we dealt with attenuation by dust continuum. Then, a method of deriving column densities of the detected COMs is shown in Section 4. The introduced method is especially useful for the wide range of line survey data. An effect of line optical depth on the column density estimation is also examined. In Section 5, we present the results of our analyses: derived COMs compositions in the V883 Ori disk, and in Section 6, we compare them with other objects and discuss the implications. Finally, we give a summary in Section 7.

2. OBSERVATION AND SPECTRAL EXTRACTION

In the ALMA Cycle 7 program 2019.1.00377.S (PI: Jeong-Eun Lee), we performed an unbiased spectral survey of V883 Ori in Band 6 with an angular resolution of $0.15''$ – $0.2''$, corresponding to ~ 60 to 80 au at a distance of 388 pc (Lee et al. 2019b). The observations were conducted between May 2021 and November 2021. The on-source integration time is 194.5 minutes. The frequency range covered by the spectral survey is 220.703 GHz to 274.861 GHz with a spectral resolution of 488.281 kHz (0.66 – 0.53 km s $^{-1}$). This spectral range is about 30 times wider than the ALMA Cycle 5 V883 Ori observation in Band 7 (Lee et al. 2019b). The continuum sensitivity is 0.01 mJy beam $^{-1}$, and the line sensitivity is 0.4 – 0.6 mJy beam $^{-1}$. The continuum emission was subtracted in the image space, and the continuum level is automatically measured using STATCONT (Sánchez-Monge et al. 2018). The dust continuum in Band 6 is less optically thick than in Band 7 by a factor of two, although the line intensity is two times stronger in Band 7. The details of observation and data reduction can be found in Lee et al. (2024, Paper I hereafter).

In V883 Ori, COMs emissions are mostly located inside the water emission region in the disk (van 't Hoff et al. 2018b; Lee et al. 2019b; Tobin et al. 2023; Yamato et al. 2024, Paper I). Figure 1 shows the emission distribution of a CH $_3$ OH line, which represents the typical emission distribution of COMs in V883 Ori. The inner emission hole of COMs ($r < \sim 0.1''$), as seen in the left panel, have been recognized in previous ALMA observations (e.g., Band 3: Yamato et al. (2024), Band 6:

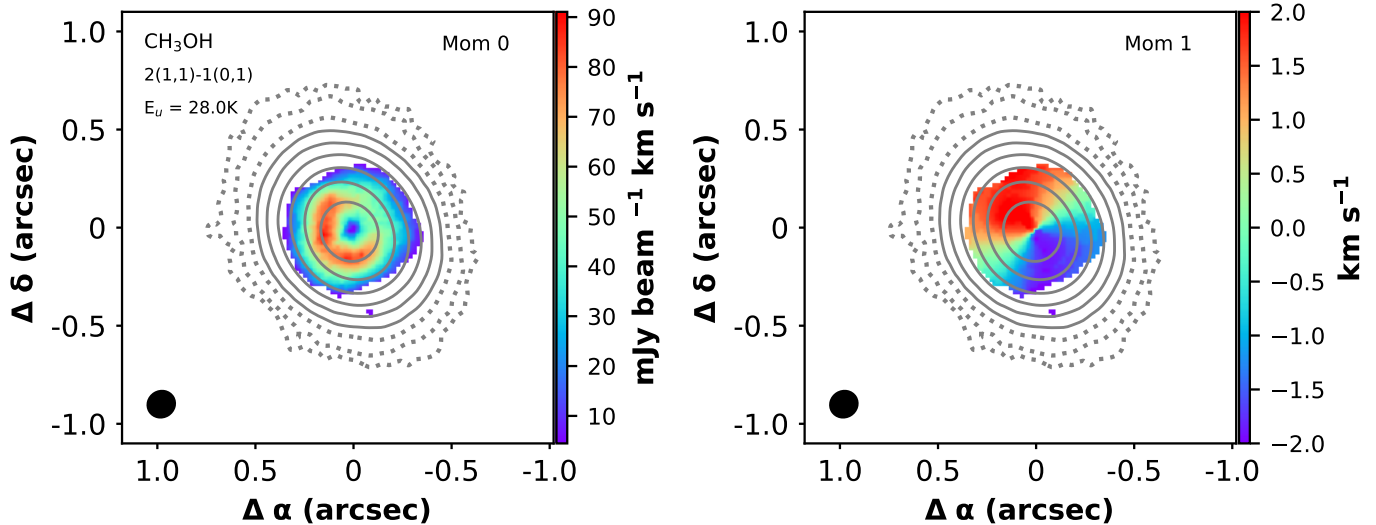


Figure 1. Integrated intensity (left panel) and intensity-weighted velocity (right panel) maps of the CH₃OH 2(1,1)-1(0,1) line, as a representative emission distribution for COMs in the V883 Ori disk. The structure in the left panel shows a ring-like shape, and the inner emission depression ($r < \sim 0.1''$) is due to the optically thick dust blocking the molecular emission. The integral of the velocity ranges from -3.5 to 3.5 km s⁻¹. The images are clipped above the 4σ ($1\sigma = 2.0$ mJy beam⁻¹) level. Black contours represent continuum emission at 5, 10, 25, 50, 100, 200, 400, 800, and 1600 σ ($1\sigma = 0.023$ mJy beam⁻¹). The three weakest black contours are shown as dotted lines, while the others are in solid lines. The beam is shown on the lower left corner of each panel. Please refer to Lee et al. (2024) (Paper I) for the analysis of the emission structure of various simple molecules as well as COMs. This figure is reproduced using the data presented in Paper I.

Tobin et al. (2023); Paper I, and Band 7: van 't Hoff et al. (2018b); Lee et al. (2019b)). This structure is due to the extremely high dust opacity toward the disk center (Cieza et al. 2016).

We extracted averaged spectra over the entire COMs emission region in the disk ($\sim 0.3''$) using a newly-developed filtering technique: first principal component (PC1) filtering method (Yun & Lee 2023). Using several strong, isolated COMs lines, Yun & Lee (2023) obtained a representative common geometric, kinematic feature of the COMs lines, a PC1, by utilizing the Principal Component Analysis (PCA) on the data cube. The PC1 was next used as a filter to apply to the 3D data cube, resulting in a PC1-filtered spectrum. This method allowed us to correct kinematic features in the disk spectrum without detailed disk kinematic modeling and, therefore, to achieve a higher signal-to-noise ratio (SNR) than a spectrum produced by the velocity alignment method (Lee et al. 2019b). For more information, please refer to Yun & Lee (2023).

The resulting full PC1-filtered spectrum is shown in the upper panel of Figure 2, and a zoomed-in portion is provided in the lower panel. The spectrum is crowded but contains well-resolved (the line width is ~ 3 km s⁻¹) rotational transition lines of molecules in the vibrational ground or excited levels.

3. SPECTRAL ANALYSES

3.1. Dust attenuation of line intensities

As seen by Lee et al. (2019b), the dust opacity affects the line intensity significantly in V883 Ori. Therefore, after the spectral extraction, we corrected the effect of dust attenuation on the intensity of the molecular lines. The observed line intensities unaffected by dust attenuation (T_{line}) can be obtained by dividing the observed continuum-subtracted intensities ($T_{\text{obs}} - T_{\text{cont}}$) by $e^{-\tau_{\nu, \text{dust}}}$ (Equation 1), where $T_{\text{cont}} \equiv \eta \times T_{\text{rot}} \times (1 - e^{-\tau_{\nu, \text{dust}}})$. Here, T_{obs} is the total observed intensity, T_{cont} is the observed continuum intensity, T_{rot} is the source function, and η is the beam-filling factor. We assume that dust and gas are well coupled and that the gas is in LTE. Therefore, T_{line} can be calculated by

$$T_{\text{line}} = \eta \times T_{\text{rot}} \times (1 - e^{-\tau_{\nu, \text{line}}}) = \frac{T_{\text{obs}} - T_{\text{cont}}}{e^{-\tau_{\nu, \text{dust}}}}. \quad (1)$$

Calculating $\tau_{\nu, \text{dust}}$ requires the molecular hydrogen column density (N_{H_2}), the dust mass opacity for a certain type of dust (κ_{ref}), and the spectral index of κ_{ref} (β), as detailed here (Equation 2).

$$\tau_{\nu, \text{dust}} = (N_{\text{H}_2} \cdot \kappa_{\text{ref}} \cdot m_{\text{H}_2} \cdot 0.01) \cdot \left(\frac{\nu}{\nu_{\text{ref}}}\right)^\beta. \quad (2)$$

We adopt $\kappa_{\text{ref}} = 2.2$ cm² g⁻¹ (at $\nu_{\text{ref}} = 230$ GHz) and $\beta = 1$ from Cieza et al. (2018). To get N_{H_2} and η , we

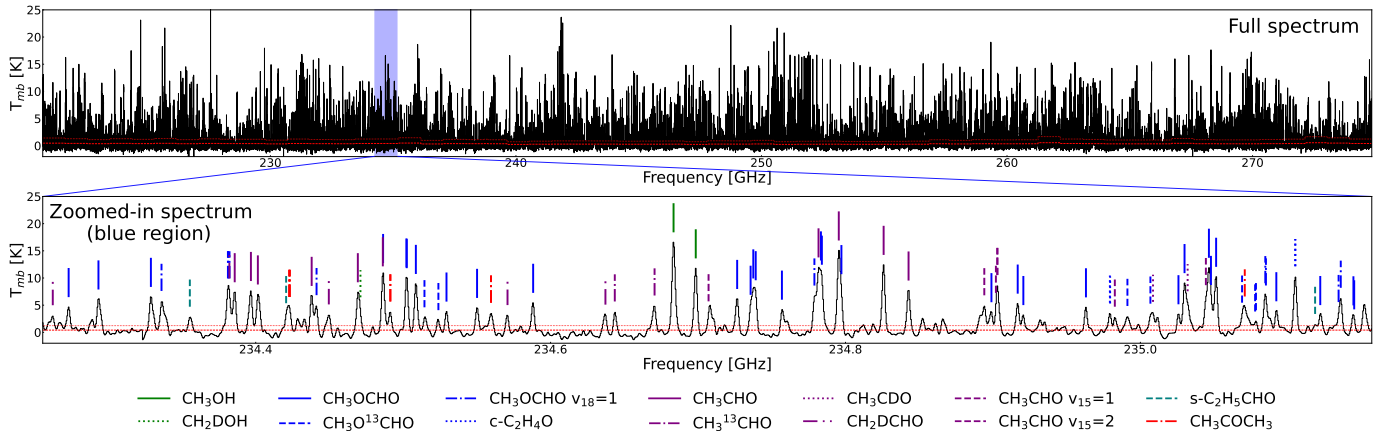


Figure 2. The disk-averaged spectrum of V883 Ori. This is the observed spectrum extracted from the PC1-filtering, but not the reconstructed one through the dust attenuation and beam-filling factor correction. The upper panel shows the spectrum of the full frequency range covered in our observation of V883 Ori, after subtraction of the continuum level. The lower panel shows a randomly selected, zoomed-in spectrum of the blue-shaded region in the upper panel. The vertical color bars represent identified lines of COMs from our study. The red dashed/dotted horizontal lines represent the $1\sigma/3\sigma$ levels of the observed spectrum.

fitted the continuum intensities as a function of spectral windows, weighted by the moment 0 map of the PC1 (Figure 3). The moment 0 map of the PC1 represents the region where the most COM emission originates (Yun & Lee 2023). To correct a systematic difference among spectra of three science goals (SGs) seen in the original reduction (Paper I), we scaled up the SG2 and SG3 spectra by 5% and 2%, respectively. Finally, the fitted η is 0.384, and the fitted N_{H_2} is $1.24 \times 10^{25} \text{ cm}^{-2}$ with uncertainty of 2%. Although $\tau_{\nu, \text{dust}}$ can vary with radius, our fitted $\tau_{\nu, \text{dust}}$ represents the averaged $\tau_{\nu, \text{dust}}$ over the COM emission region ($\sim 0.1''$ to $\sim 0.3''$; Paper I), and it is appropriate for the dust attenuation correction of the PC1-filtered spectra. Also, there is no notable size variation of the optically thick region ($\sim 0.1''$) across our frequency range.

According to the calculation, the observed line intensities ($T_{\text{obs}} - T_{\text{cont}}$, Figure 2) are reduced to 34% – 42% of the dust-corrected values (T_{line}) over the observed frequency range. We used these corrected spectra throughout our analyses with molecular line identification and iterative LTE line fitting. However, the spectra shown in the figures in this paper (Figure 2, 4 and 15) are presented using the originally observed PC1-filtered spectra ($T_{\text{obs}} - T_{\text{cont}}$), not the reconstructed ones.

3.2. Molecular line identification

To investigate the chemical composition of the disk, the first step is to identify which molecules produce the observed lines. We used the eXtended CASA Line Analysis Software Suite (XCLASS, Möller et al. 2017) for the line identification. Assuming local thermodynamic equilibrium (LTE), XCLASS can model the spectra of each

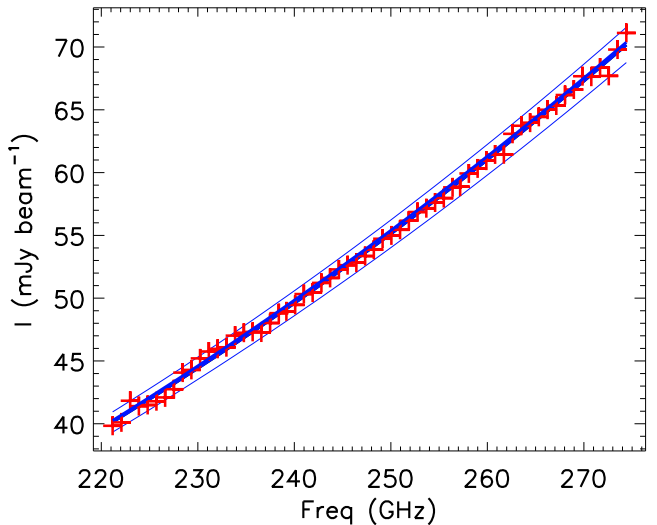


Figure 3. The continuum intensities as a function of spectral window weighted by the moment 0 map of the PCA Eigen cube 1. The red crosses indicate the corrected intensity of each spectral window. The thick blue line is the best-fit result of $T_{\text{cont}} \equiv \eta \times T_{\text{rot}} \times (1 - e^{-\tau_{\nu, \text{dust}}})$. The thin blue lines represent $\pm 2\%$ range.

molecular species by managing several parameters, such as velocity width (v_{width}), rotation temperature (T_{rot}), column density (N), and beam-filling factor (η).

To simplify the analysis, N was used as the only free parameter. We fixed v_{width} at 3 km s^{-1} , which is obtained from the PC1-filtered spectrum. T_{rot} was set to 120 K, which is the average temperature within $0.3''$ radius of the disk model of V883 Ori (Lee et al. 2019b). The radius of $0.3''$ corresponds to the representative

COMs emission size (moment 0 map of PC1) in V883 Ori (Yun & Lee 2023). We fixed η at 0.384, which was estimated from the continuum fitting after weighting with the moment 0 map of PC1 (Figure 3). This value is consistent with the one derived from the optically thick, saturated CH₃OH lines, as the strongest CH₃OH line shows the closest correlation with PC1 (Yun & Lee 2023). After correcting for dust attenuation, the intensities of the optically thick CH₃OH lines are ~ 46 K, which corresponds to 0.384 times the source function (120 K).

XCLASS uses the molecular databases from both Cologne Database for Molecular Spectroscopy (CDMS) (Müller et al. 2001, 2005) and Jet Propulsion Laboratory (JPL) (Pickett et al. 1998). CDMS and JPL databases contain about 1,500 molecules (ranging from simple molecules to COMs) that emit at least one molecular line in our observed spectral windows.

Due to the densely populated energy states of COMs compared to the simple molecules, COMs can emit numerous transition lines across the frequency range of this observation. In addition, with 1,500 species to consider, multiple candidate molecules may be assigned for a single emission line, which makes the line identification more complicated. Therefore, to properly identify the observed lines, we created a model spectrum with the myXCLASS function within XCLASS for individual test species. Then, we checked whether the frequencies of all modeled transitions of the test species matched the frequencies of the observed lines within the spectral resolution.

The left and middle panels of Figure 4 show examples of model spectra compared to observed spectra. Among the four cases (model spectra in green, red, blue, and purple) in the figure, only the model for acetone (CH₃COCH₃), modeled with an input column density of 5×10^{16} cm⁻² (red solid lines in the left panel), matches the observation. On the other hand, the acetone model with a column density of 5×10^{18} cm⁻² (green solid line in the left panel) only provides a partial match. In this case, it is possible to make a misidentification of an observed line as acetone, such as a line near 239.02 GHz. Lastly, in the case of glycolaldehyde (CH₂OHCHO) in the middle panel, neither of the two cases (blue and purple solid lines) can successfully identify the observed lines. Therefore, it is important to use both the correct species and the appropriate column density for the line identification, as Jørgensen et al. (2020) pointed out.

Thus, for every possible species (about 1,500), we constructed model spectra with 35 column density steps (from 5×10^{12} cm⁻² to 5×10^{18} cm⁻²). Then, we defined a simple parameter $f_{N,X}$ (Equation 3) and calculated it for all model spectra at each column density (N) step

and species (X), so that we could readily filter for strong candidate molecules.

$$f_{N,X} \equiv \frac{\# \text{ of observed lines matched with model}}{\# \text{ of modeled lines}} \quad (3)$$

For example, in the frequency range corresponding to the x-axis of the left panel of Figure 4, the value of $f_{N,X}$ for acetone would be 3/3 (100%) at $N=5 \times 10^{16}$ cm⁻² and 5/8 (62%) at $N=5 \times 10^{18}$ cm⁻². Thus, the former model spectrum can be adopted as the acetone line identification.

The right panel of Figure 4 shows the $f_{N,X}$ profiles for 10 test molecules *over the entire frequency range* of the spectral survey. These $f_{N,X}$ were automatically calculated using the lines regardless of line intensity if the intensities are above the 3σ levels. From the $f_{N,X}$ profiles in the figure, we can consider CH₃OH, c-C₂H₄O, CH₃CHO, CH₃COCH₃, CH₃OCHO, and CH₃CN as strong candidates for molecules present in V883 Ori, whereas CH₃COOH, CH₂OHCHO, CH₃OCH₂OH, and NH₂CHO can be ruled out as non-detections.

We, therefore, collected molecules that reached 100% of $f_{N,X}$ at some column density steps among the 1,500 species. Usefully, $f_{N,X}$ decreases after reaching 100% because the model lines with higher column densities overproduce non-detected weak lines, as illustrated by the CH₃COCH₃ model with 5×10^{18} cm⁻² (the green spectra in the left panel). Finally, we performed a visual inspection to confirm the detection of those molecules selected by this procedure. Furthermore, for the species with relatively high $f_{N,X}$ still below 100%, we retested using finer column density steps and detected a few more species.

4. THE LTE ANALYSES OF COMS

4.1. Column density estimation with an iterative LTE line fitting

For the detected molecules, we derive the average column densities over the COMs-emission region in the disk of V883 Ori using an LTE line fitting tool. In this section, we describe the method, and the results are presented in Section 5.

We fitted the observed lines with the model spectra of each detected species individually by adjusting the input parameters for the model spectra; the results are independent of other species because we use only isolated and optically thin lines, excluding the blended lines in our iterative line fitting process. As mentioned in the previous section, the column density (N) was the only free parameter in the analysis, while the other parameters were fixed to the aforementioned values. We operated a fitting tool of XCLASS: the Modeling and Analysis

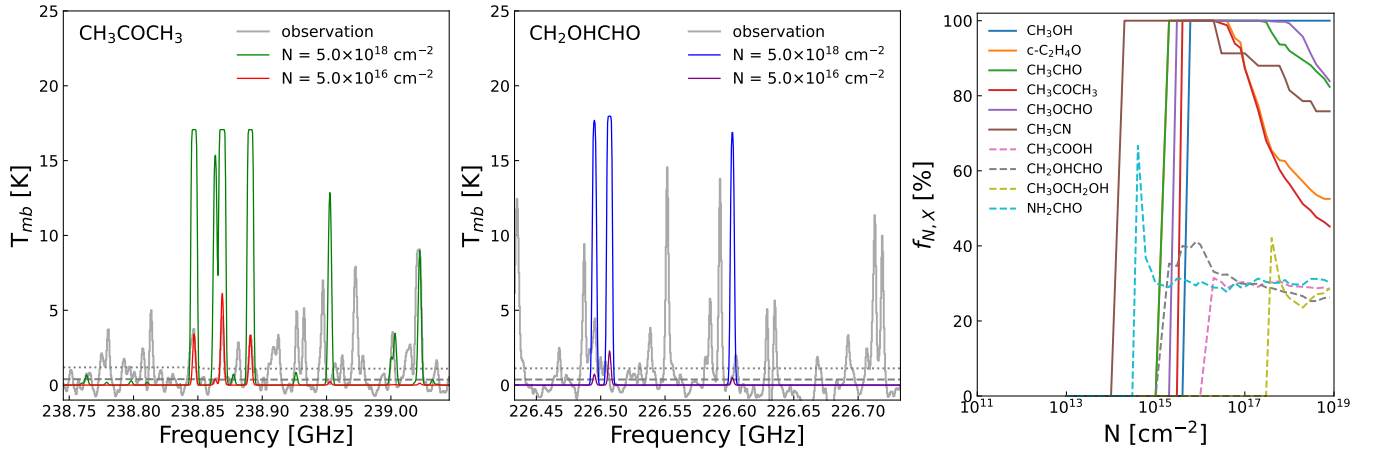


Figure 4. Figures to depict the line identification method. Left and middle panels: Four examples for XCLASS model spectra, overlaid on the observed spectra. The colored solid lines indicate acetone (CH_3COCH_3) and glycolaldehyde (CH_2OHCHO) model spectra at two different column densities ($N=5.0 \times 10^{18} \text{ cm}^{-2}$, $5.0 \times 10^{16} \text{ cm}^{-2}$), respectively. The gray solid lines are the observed spectra and gray dashed/dotted horizontal lines represent the $1\sigma/3\sigma$ levels of the observed spectrum. Right panel: As examples for $f_{N,X}$ (Equation 3), we show the $f_{N,X}$ profiles for 10 molecules. The profiles are shown as solid lines for the six molecules whose ratios reached 100% (considered as detected) at some column density steps, and as dashed lines for the remaining four molecules.

Generic Interface for eXternal numerical codes (MAGIX) (Möller et al. 2013). The genetic algorithm was used to derive the best-fit values of the parameters, and the Markov chain Monte Carlo (MCMC) method was used to calculate the uncertainties. These algorithms are available as part of MAGIX.

The spectra were extracted over the COMs emission region, which is the dense inner disk. Therefore, the spectra contain optically thick lines, which must be excluded in the fitting process to accurately estimate column densities (e.g., Jørgensen et al. (2018); Drozdovskaya et al. (2022)). However, since we do not know which lines are optically thick in the first place, we repeated the line fitting, removing lines with an optical depth higher than a certain value and, thus, utilizing only the optically thin lines at each iteration.

Here, we present a simple algorithm for this iterative line-fitting method. First, we fitted an LTE model spectrum of each molecular species over the full observed spectra for all detected molecules, individually, regardless of line optical depths at the line center ($\tau_{\nu,\text{line}}$). Second, we calculated the line optical depths from the first fitted model spectrum for each species. We then collected observed lines, which are optically thin and well isolated in the model. In addition, we removed observed lines with large line width ($> 4 \text{ km s}^{-1}$), which may be due to blending with unidentified lines. These collected lines of each molecule were used for the next fitting process. Then again, isolated, optically thin lines were re-collected from these new results. This fitting process was done iteratively until the best-fit value of

the column densities converged. This approach using only optically thin, isolated lines is possible because we identified as many molecular lines as possible during the line identification process, in addition to the broad frequency coverage of our spectral line survey.

The optical depth criterion is set to $\tau_{\nu,\text{line}} = 0.7$, meaning that only lines with their modeled $\tau_{\nu,\text{line}}$ lower than 0.7 are considered in the fitting process. We adopt 0.7 because lowering the criterion below 0.7 reduces the number of lines available for fitting, and the selected lines have overall lower signal-to-noise ratios. For example, if we take the optical depth criterion as 0.2, the signal-to-noise ratios of the lines are mostly in the range of 3–5, and the number of lines used for fitting is reduced by about a factor of two, compared to the case of 0.7.

Two examples of column densities obtained from the iterative fitting method are presented in Figure 5. These two molecules ($^{13}\text{CH}_3\text{OH}$ and CH_3OCHO) are exemplary of the molecules emitting mostly optically thin lines and the molecules emitting many optically thick lines, respectively. The column density of the former case ($^{13}\text{CH}_3\text{OH}$) remains nearly constant through the iteration because only few optically thick lines, out of 41 isolated lines, are excluded from the fit, i.e., most of the lines are optically thin.

On the other hand, the column density of the latter case (CH_3OCHO) gradually increases from $3.15 \times 10^{17} \text{ cm}^{-2}$ and converges to $1.05 \times 10^{18} \text{ cm}^{-2}$, which is about three times larger than the result of 0th iteration. The number of isolated and optically thin lines of CH_3OCHO

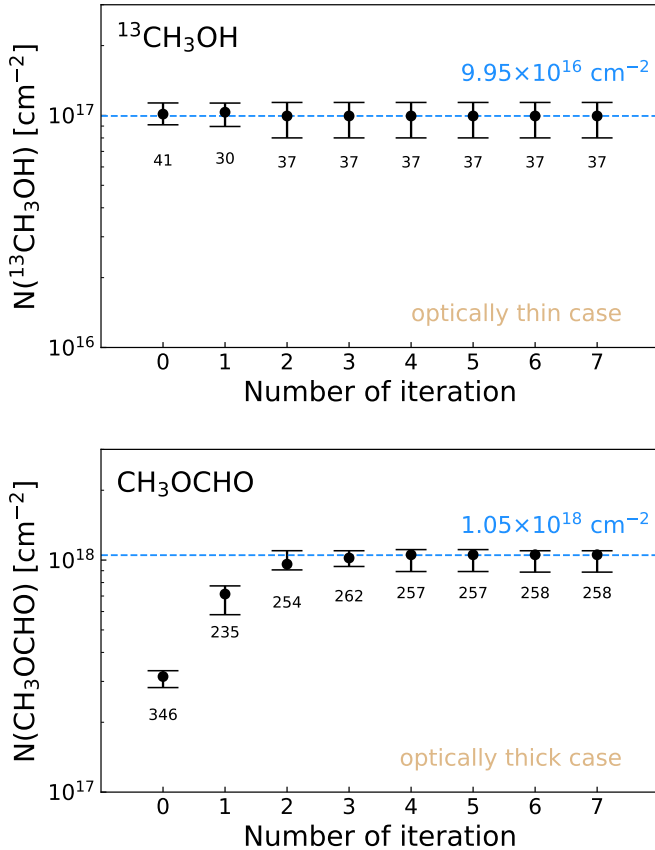


Figure 5. Examples of iterative LTE line fitting results on a molecule that emits mostly optically thin lines ($^{13}\text{CH}_3\text{OH}$), and several optically thick lines (CH_3OCHO). The 0th iteration indicates the fitting result when using the isolated lines without optical depth consideration. The remaining iterations show the results of the fitting using optically thin ($\tau_{\nu,\text{line}} < 0.7$), isolated lines extracted from the results of the previous iteration. The numbers under data points are the number of isolated molecular lines used in the LTE fitting in that iteration. The number in the upper right of each figure is the column density obtained as the final result of this method, which is also drawn as a blue horizontal dashed line.

increases as the column density increases because unseen lines in the model with smaller column densities become more prominent as the column density increases. The fitted column density increases as new optically thin lines are included and new optically thick lines are excluded at the next iteration. The number of used isolated lines decreases from 346 (in iteration 0) to 235 (in iteration 1) because iteration 0 uses isolated lines from all $\tau_{\nu,\text{line}}$ ranges. In contrast, iteration 1 uses isolated lines with $\tau_{\nu,\text{line}} < 0.7$. Also, some lines turn out to be blended, which reduces the number of isolated lines itself. This is due to newly populated lines from other molecules whose column density is increased.

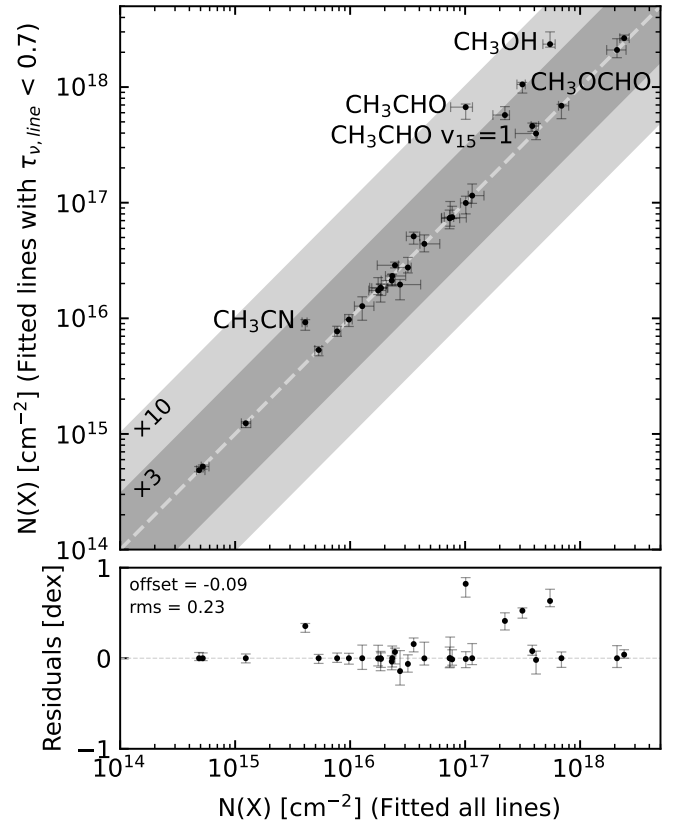


Figure 6. Comparison of the column densities of molecules obtained by iterative LTE line fitting using only isolated, optically thin lines ($\tau_{\nu,\text{line}} < 0.7$, corresponds to the column density result of the 7th iteration of Figure 5) and using isolated lines of all optical depths (corresponds to the result of the 0th iteration of Figure 5). Each data point represents the derived column densities of a single species. Labeled molecules are the ones that show differences of larger than 0.2 dex. The line representing 1:1 is indicated by a gray dashed line. The lines representing 3 times and 10 times differences are shown as gray solid lines with dark and light gray shaded areas, respectively.

Lastly, for the molecules that were not detected in V883 Ori, we obtained upper limits on their column densities to compare with previous studies on COMs. The column density producing the strongest line corresponding to the 3σ level of the observation is considered the upper limit.

To validate our estimation of molecular column densities via iterative LTE line fitting, we also utilized a rotation diagram method, a simpler LTE analysis. We described the results and implications from the rotation diagram analysis in Appendix A. In short, the difference in column densities obtained from the two methods has a scatter of 0.28 dex with only a slight offset of 0.03 dex.

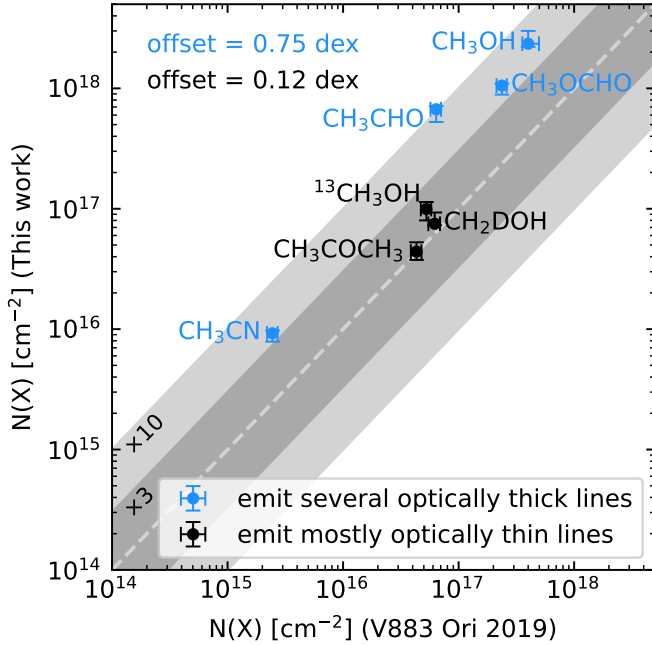


Figure 7. The estimated column density results from 2019 V883 Ori (Lee et al. 2019b) compared to those derived in this work (Table 1, y-axis of Figure 6). The data points are from the Supplementary Table 1 by Lee et al. (2019b). The gray dashed line represents the one-to-one line. The lines representing 3 times and 10 times difference from the one-to-one values are shown as solid gray lines with dark and light gray shaded areas, respectively.

4.2. Line optical depth effects on column density estimation

In this section, we quantitatively investigate the effect of the line optical depth in estimating column density by comparing two cases (1) only with optically thin lines and (2) with all lines.

Figure 6 compares the estimated column density results for the two cases. Most molecules are aligned along a one-to-one line, so the resulting column densities of the two approaches are likely to be consistent. However, for some molecules such as methanol (CH_3OH), methyl formate (CH_3OCHO), and acetaldehyde (CH_3CHO), the latter method underestimates the column density by up to almost an order of magnitude compared to the former. These are the molecules whose column densities tend to increase as the iterations continue and converge to a particular value during the iterative fitting process, as shown in the example on the lower panel of Figure 5. Note that even vibrationally excited molecules like $\text{CH}_3\text{CHO } \nu_{15}=1$ can emit optically thick lines, and their column density can be therefore underestimated. In Appendix B, we examine in more detail the optical depth effect in the modeling of observed spectra.

Furthermore, we compared the column densities from this work to the column densities by Lee et al. (2019b) that used the ALMA Band 7 spectra of V883 Ori (see Figure 7). Previously, due to the small frequency range of the observation, it was impossible to do selective line fitting using only isolated, optically thin lines. Therefore, Figure 7 shows that the values from Lee et al. (2019b) follow the same tendency as seen in Figure 6. The column densities of molecules emitting optically thick lines are underestimated by an average difference of 0.75 dex, or 5.6 times, while molecules emitting mostly optically thin lines have similar best-fit column densities with an average difference of 0.12 dex, compared to the values derived from only optically thin lines by this work. For example, the derived column density of CH_3OH is 5.9 times higher than that in Lee et al. (2019b).

The above comparisons demonstrate that the wide frequency coverage obtained by this spectral survey is critical for accurate column density estimation with a sufficient number of optically thin lines. Moreover, the iterative LTE line fitting method allows us to effectively exclude optically thick lines that can lead to underestimating the column densities.

5. RESULTS

In this paper, we present the analysis results of only COMs, although we have identified lines from simple molecules as well as COMs to extract isolated lines properly in the procedures of line identification and column density estimation described in previous sections.

5.1. COMs detected in the disk of V883 Ori

As a result of the line identification, a total of 23 complex organic molecular species have been found in V883 Ori, based on about 3,700 lines above 3σ . Most observed lines have been identified, but $\sim 20\%$ of the lines remain unidentified. Many of these unidentified lines lack corresponding line information in the databases we adopted. Therefore, updated spectroscopic databases are necessary to identify the remaining lines. The spectroscopic data from direct spectroscopic experiments (e.g., Ohno et al. 2022; Müller et al. 2023; Ferrer Asensio et al. 2023; Oyama et al. 2023) could be adopted, but we leave this as a future work.

Table 1 lists all detected COMs and their column densities obtained through the iterative LTE line fitting method. The 23 species consist of 11 main isotopologues, with the remaining 12 composed of various ^{13}C , ^{18}O isotopologues, and deuterated molecules.

This plethora of identified COMs demonstrates that the disk of V883 Ori is as chemically rich as the Class 0

hot cores (Belloche et al. 2016; Baek et al. 2022; Chen et al. 2023) and hot corinos (Drozdovskaya et al. 2019; Hsu et al. 2022). However, for V883 Ori oxygen-bearing COMs were exclusively detected, especially molecules containing one oxygen. Methyl formate (CH_3OCHO) is the only detected molecule that contains two oxy-

gen atoms. On the other hand, although numerous detectable lines of nitrogen-bearing COMs are covered in the frequency range, only methyl cyanide (CH_3CN) was detected in this disk.

Table 1. List of all COMs detected in V883 Ori with minimum line information and column densities from the LTE line fitting analysis.

No.	Species	# of lines ^a	E_u (K)	N (cm^{-2})	No.	Species	# of lines	E_u (K)	N (cm^{-2})
Methanol					$\text{CH}_3^{13}\text{CHO } v_{15}=1$				
1	CH_3OH	102 (20)	20.1 - 926.6	$2.35^{+0.65}_{-0.14} \times 10^{18}$	12	CH_3CDO	86 (41)	74.5 - 233.4	$9.75^{+1.03}_{-1.25} \times 10^{15}$
	$\text{CH}_3\text{OH } v_{12}=1$	25 (13)	326.2 - 771.0	$2.65^{+0.17}_{-0.10} \times 10^{18}$	13	CH_2DCHO	126 (67)	73.0 - 294.3	$2.12^{+0.27}_{-0.20} \times 10^{16}$
	$\text{CH}_3\text{OH } v_{12}=2$	9 (1)	542.9 - 717.5	$2.09^{+0.53}_{-0.30} \times 10^{18}$	Ethanol				
2	$^{13}\text{CH}_3\text{OH}$	68 (37)	19.9 - 480.3	$9.95^{+1.43}_{-1.95} \times 10^{16}$	14	$\text{C}_2\text{H}_5\text{OH}$	51 (37)	28.5 - 216.4	$2.75^{+0.61}_{-0.28} \times 10^{16}$
3	$\text{CH}_3^{18}\text{OH}$	29 (16)	33.4 - 196.9	$7.33^{+1.30}_{-1.38} \times 10^{16}$	Propanal				
4	CH_2DOH	87 (47)	22.6 - 347.1	$7.50^{+1.81}_{-0.21} \times 10^{16}$	15	$s\text{-C}_2\text{H}_5\text{CHO}$	206 (87)	41.0 - 302.3	$2.87^{+0.19}_{-0.15} \times 10^{16}$
Methyl formate					Propyne				
5	CH_3OCHO	676 (258)	36.3 - 1391.0	$1.05^{+0.04}_{-0.17} \times 10^{18}$	16	CH_3CCH	16 (8)	74.6 - 176.6	$1.27^{+0.26}_{-0.31} \times 10^{16}$
	$\text{CH}_3\text{OCHO } v_{18}=1$	265 (198)	220.2 - 740.9	$6.89^{+0.20}_{-1.56} \times 10^{17}$	Dimethyl ether				
6	$\text{CH}_3\text{O}^{13}\text{CHO}$	177 (70)	36.0 - 295.9	$7.42^{+2.83}_{-1.16} \times 10^{16}$	17	CH_3OCH_3	292 (32)	21.8 - 1882.4	$4.60^{+0.28}_{-0.48} \times 10^{17}$
Ethylene oxide					Acetone				
7	$c\text{-C}_2\text{H}_4\text{O}$	40 (23)	31.5 - 495.4	$5.12^{+0.45}_{-0.74} \times 10^{16}$	18	CH_3COCH_3	187 (108)	34.2 - 997.3	$4.40^{+0.86}_{-0.65} \times 10^{16}$
8	$c\text{-C}^{13}\text{CH}_4\text{O}$	13 (5)	34.9 - 64.0	$5.32^{+0.38}_{-0.58} \times 10^{15}$	2-Propenal				
Acetaldehyde					Methyl cyanide				
9	CH_3CHO	313 (74)	18.3 - 775.9	$6.70^{+0.43}_{-1.44} \times 10^{17}$	19	$\text{C}_2\text{H}_3\text{CHO}$	96 (44)	46.7 - 410.4	$7.71^{+0.83}_{-0.72} \times 10^{15}$
	$\text{CH}_3\text{CHO } v_{15}=1$	193 (54)	224.6 - 1007.9	$5.73^{+1.05}_{-0.49} \times 10^{17}$	20	CH_3CN	19 (4)	68.9 - 442.4	$9.23^{+0.51}_{-1.35} \times 10^{15}$
	$\text{CH}_3\text{CHO } v_{15}=2$	87 (47)	439.5 - 975.3	$3.97^{+0.88}_{-0.46} \times 10^{17}$		$\text{CH}_3\text{CN } v_8=1$	20 (7)	588.0 - 679.2	$2.32^{+0.10}_{-0.42} \times 10^{16}$
10	$^{13}\text{CH}_3\text{CHO}$	95 (67)	70.2 - 828.0	$1.82^{+0.15}_{-0.25} \times 10^{16}$	21	$^{13}\text{CH}_3\text{CN}$	12 (9)	78.0 - 167.3	$5.23^{+0.16}_{-0.27} \times 10^{14}$
	$^{13}\text{CH}_3\text{CHO } v_{15}=1$	18 (11)	286.1 - 366.9	$1.84^{+0.14}_{-0.46} \times 10^{16}$	22	$\text{CH}_3^{13}\text{CN}$	8 (4)	80.3 - 156.9	$4.86^{+0.37}_{-0.15} \times 10^{14}$
11	$\text{CH}_3^{13}\text{CHO}$	89 (54)	71.1 - 275.2	$1.74^{+0.51}_{-0.14} \times 10^{16}$	23	CH_2DCN	24 (7)	75.8 - 294.0	$1.24^{+0.04}_{-0.10} \times 10^{15}$

^aThe number of all identified lines over 3σ noise level. In parentheses is the number of isolated, optically thin molecular lines used in the LTE line fitting.

To find clues about the formation pathways of the molecules, we organized the observed COMs in V883 Ori to see if their isomers were also found (see Table 2). Among molecules listed in Table 2, five isomers were undetected in V883 Ori. Propadiene, vinyl alcohol, and propylene oxide are detected only in limited astrophysical objects. Propadiene has only been revealed in the atmosphere of Titan (Lombardo et al. 2019), and vinyl alcohol detection has been reported in the high-mass star-forming region Sagittarius B2(N) (Turner & Apponi 2001), the starless core TMC-1 (Agúndez et al. 2021), and the giant molecular cloud G+0.693-0.027 (Jiménez-Serra et al. 2022). Propylene oxide, an isomer of propanal and acetone, was discovered only in an extended molecular shell around the protostellar clusters in the star-forming region of Sagittarius B2

(McGuire et al. 2016). On the other hand, the two isomers of methyl formate (glycolaldehyde and acetic acid) are more commonly detected than the above-mentioned COMs in various star-forming regions (Hollis et al. 2001; Jørgensen et al. 2016; Ceccarelli et al. 2023). However, despite the possibility of several emission lines of the two isomers within our observed frequency range, they were not detected.

5.2. Column densities of the detected molecules

Figure 8 shows a bar plot displaying the column densities listed in Table 1. The column densities span several orders of magnitude, with values that fall into two main groups based primarily on main isotopologues: CH_3OH , CH_3CHO , CH_3OCH_3 , and CH_3OCHO are the abundant species with column densities of 10^{17} – 10^{18} cm^{-2} , while CH_3CCH , CH_3CN , $c\text{-C}_2\text{H}_4\text{O}$, $\text{C}_2\text{H}_5\text{OH}$, $\text{C}_2\text{H}_3\text{CHO}$, s -

Table 2. Isomers of detected COMs in V883 Ori, with the detection information in other star-forming regions (SFRs).

Formula	Isomer	Detection	
		V883 Ori	SFRs
C ₃ H ₄	CH ₃ CCH (Propyne)	Yes	Yes
	CH ₂ CCH ₂ (Propadiene)	No	No
C ₂ H ₄ O	c-C ₂ H ₄ O (Ethylene oxide)	Yes	Yes
	CH ₃ CHO (Acetaldehyde)	Yes	Yes
	CH ₂ CHOH (Vinyl alcohol)	No	Yes
C ₂ H ₆ O	CH ₃ OCH ₃ (Dimethyl ether)	Yes	Yes
	C ₂ H ₅ OH (Ethanol)	Yes	Yes
C ₃ H ₆ O	s-C ₂ H ₅ CHO (Propanal)	Yes	Yes
	CH ₃ COCH ₃ (Acetone)	Yes	Yes
	CH ₃ CHCH ₂ O (Propylene oxide)	No	Yes
C ₂ H ₄ O ₂	CH ₃ OCHO (Methyl formate)	Yes	Yes
	CH ₂ OHCHO (Glycolaldehyde)	No	Yes
	CH ₃ COOH (Acetic acid)	No	Yes

C₂H₅CHO, and CH₃COCH₃ exhibit relatively small column densities of about 10¹⁶ cm⁻².

The column densities obtained from transitions in a vibrationally excited state (e.g., CH₃OH v₁₂=1) represent the total number of the molecule (e.g., CH₃OH as a whole), not the number of molecules in that particular excited state. Therefore, the column densities estimated from the rotational transitions, both in the vibrationally ground state and in the excited state, must be consistent within fitting errors, like in the case of CH₃OH.

However, there are exceptions (CH₃OCHO v₁₈=1, CH₃CHO v₁₅=2, and CH₃CN v₈=1) that show differences in derived column densities by up to a factor of 2 when compared with their lower vibrational energy levels. The excitation to the higher vibrational energy states requires hotter and denser conditions. Therefore, the transitions in vibrationally excited states may originate from hotter regions of the disk such as its upper atmosphere. In Appendix A.3, we test hotter temperature conditions to show that the column densities of the vibrationally excited species derived from a higher temperature of 200 K better match with the 120 K derived column densities of the ground state species. In addition, we demonstrate that a fixed rotation temperature of 120 K is more appropriate than higher temperatures (200 K, 300 K) for most species.

6. DISCUSSION

6.1. Comparisons with other sources

This section presents comparisons of the chemical composition of several different young stellar objects, as well as a Solar System comet. A comparison of the abundances relative to methanol (i.e., N(X)/N(CH₃OH)) of

all main isotopologues detected in V883 Ori, along with the upper limits for some undetected species, against two representative sources is presented in Section 6.1.1. A comparison with a number of sources, but for a few molecules, is presented in Section 6.1.2. The comparison results show that V883 Ori disk exhibits unique characteristics that set it apart from other targets.

6.1.1. Comparisons against a hot corino and a comet

We compare the COMs composition of the V883 Ori disk against the compositions of a Class 0 hot corino IRAS 16293-2422 and a Solar System comet 67P/Churyumov–Gerasimenko (hereafter 67P/C-G), each representing, respectively, an earlier and more evolved stage than V883 Ori.

IRAS 16293-2422 is a Class 0 low-mass protostellar binary system (IRAS 16293-2422A and IRAS 16293-2422B) with a projected separation of 747 au. It is located in the Ophiuchus cloud complex at a distance of 141 pc (Jørgensen et al. 2016; Dzib et al. 2018; Drozdovskaya et al. 2019). IRAS 16293-2422 has been studied with an unbiased ALMA spectral survey, Protostellar Interferometric Line Survey (PILS, Jørgensen et al. (2016)), which covers about 35 GHz wide frequency range in Band 7. Various COMs were detected by identifying over 10,000 lines in this Class 0 hot corino (Jørgensen et al. 2020). Thus, the PILS survey is a good reference for comparing chemical properties in detail with this study.

In Appendix D we tabulate a detailed comparison of the column densities of COMs and their column density relative to CH₃OH between V883 Ori and IRAS 16293-2422 (Table 5). For this comparison, we used the results of IRAS 16293-2422B in the IRAS 16293-2422 binary system. For 40 species including isotopologues that are not detected in V883 Ori, we present the upper limits of column densities, which are those column densities when their maximum intensities of the model spectra correspond to the 3σ levels of the observations.

Overall, more diverse main isotopologues of COMs were detected in IRAS 16293-2422B than V883 Ori. In addition, all the main COMs detected in V883 Ori are also present in IRAS 16293-2422B. Table 3 lists COMs found only in IRAS 16293-2422B with non-detection in V883 Ori. Glycolaldehyde and its isomer, acetic acid, and its reduced alcohol, ethylene glycol, were not detected in V883 Ori. Most of them are molecules containing the hydroxymethyl group (CH₂OH). In addition, the nitrogen-bearing molecules, except for CH₃CN, are also missing in V883 Ori. We discuss implications of the non-detections of CH₂OH-, nitrogen-bearing COMs in Section 6.2.

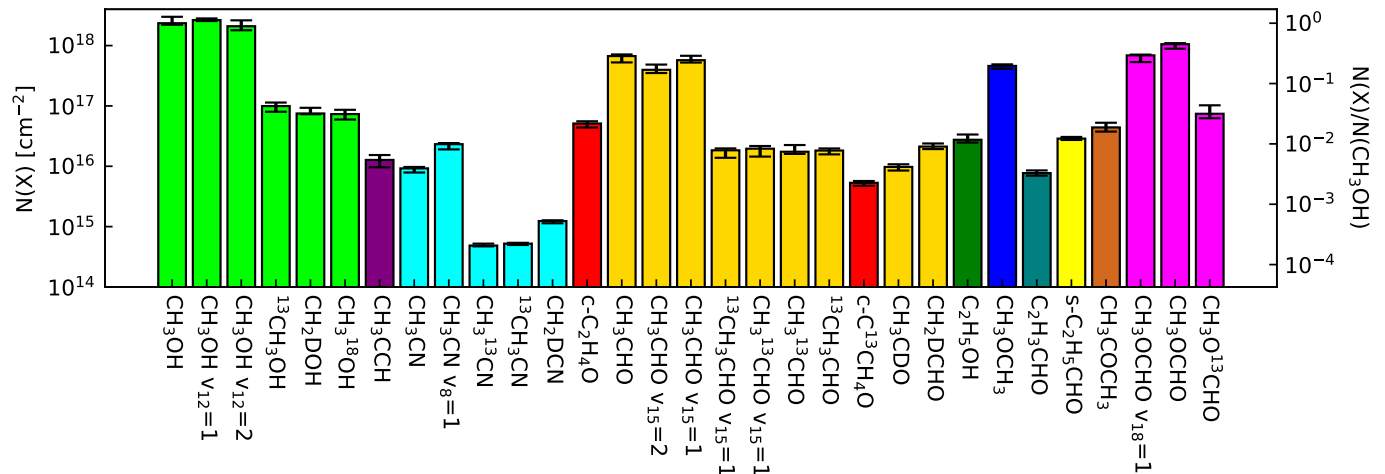


Figure 8. Bar plot for the (relative) column densities of all the COMs detected in V883 Ori. The column density values are from Table 1. COMs are sorted by increasing the value of mass, and the same color indicates isotopologues of the same species. The error bars are the uncertainties in the column densities, not the relative column densities.

We plot a diagram for abundances relative to methanol to compare these two sources (Left panel of Figure 9), along with upper limits of the species listed in Table 3. The oxygen-bearing COMs in V883 Ori are generally more abundant than those in IRAS 16293-2422B, with abundances more than an order of magnitude higher. The molecule with the largest difference is 2-propenal (C_2H_3CHO), which shows two orders of magnitude difference. However, ethanol (C_2H_5OH) shows a smaller abundance in V883 Ori than IRAS 16293-2422B, by about a factor of two. Among the undetected molecules in V883 Ori, the upper limit of glycolaldehyde (CH_2OHCHO) and formamide (NH_2CHO) are several times less than the abundances of IRAS 16293-2422B. The only detected nitrogen-bearing molecule in V883 Ori is methyl cyanide (CH_3CN), whose abundance is comparable with IRAS 16293-2422B. Therefore, the abundances of the detected COMs in the V883 Ori disk are overall higher than those of the Class 0 hot corino IRAS 16293-2422B, still with a positive correlation. However, ethanol and methyl cyanide deviate from the correlation and have similar abundances in these two targets.

We also make a comparison of the compositions with Comet 67P/C-G, a Jupiter family comet visited by the Rosetta Mission. Through the mission, various organic compounds were discovered, and their abundances were determined (Schuhmann et al. 2019; Rubin et al. 2019). The cometary values were presented and compared with the abundances of Class 0 hot corino IRAS 16293-2422B in a study by Drozdovskaya et al. (2019). They revealed that the CHO-, nitrogen-bearing COMs in 67P/C-G

Table 3. COMs undetected in V883 Ori but detected in IRAS 16293-2422B.

Species	Formula	Species	Formula
Acetic acid	CH_3COOH	Methyl isocyanide	CH_3NC
Glycolaldehyde	CH_2OHCHO	Formamide	NH_2CHO
Ethylene glycol	$(CH_2OH)_2$	Methyl isocyanate	CH_3NCO
Methoxymethanol	CH_3OCH_2OH	Vinyl cyanide	C_2H_3CN
		Ethyl cyanide	C_2H_5CN

have higher abundances systematically, but still with a good correlation between the two sources.

The right panel of Figure 9 shows the abundances of COMs detected in V883 Ori and 67P/C-G. Abundances in the two objects are consistent without any obvious offset, although the CH_3OCHO and CH_3CN abundances in V883 Ori are higher and lower, respectively, by an order of magnitude than in the comet.

The higher abundances than the Class 0 hot corino and similar abundances with the cometary ices may indicate the possibility of in-situ chemical evolution in a disk around a young star rather than maintaining the original compositions from the protostellar envelope.

6.1.2. Comparisons against various sources

For a few COMs, we show an additional comparison with various studies of Class 0/I hot corinos, including the ALMA/PILS (Jørgensen et al. 2016), IRAM/CALYPSO (Belloche et al. 2020), ALMA/PEACHES (Yang et al. 2021), ALMA/ALMASOP (Hsu et al. 2022), and the ALMA observation of HOPS 373SW, which is a very young

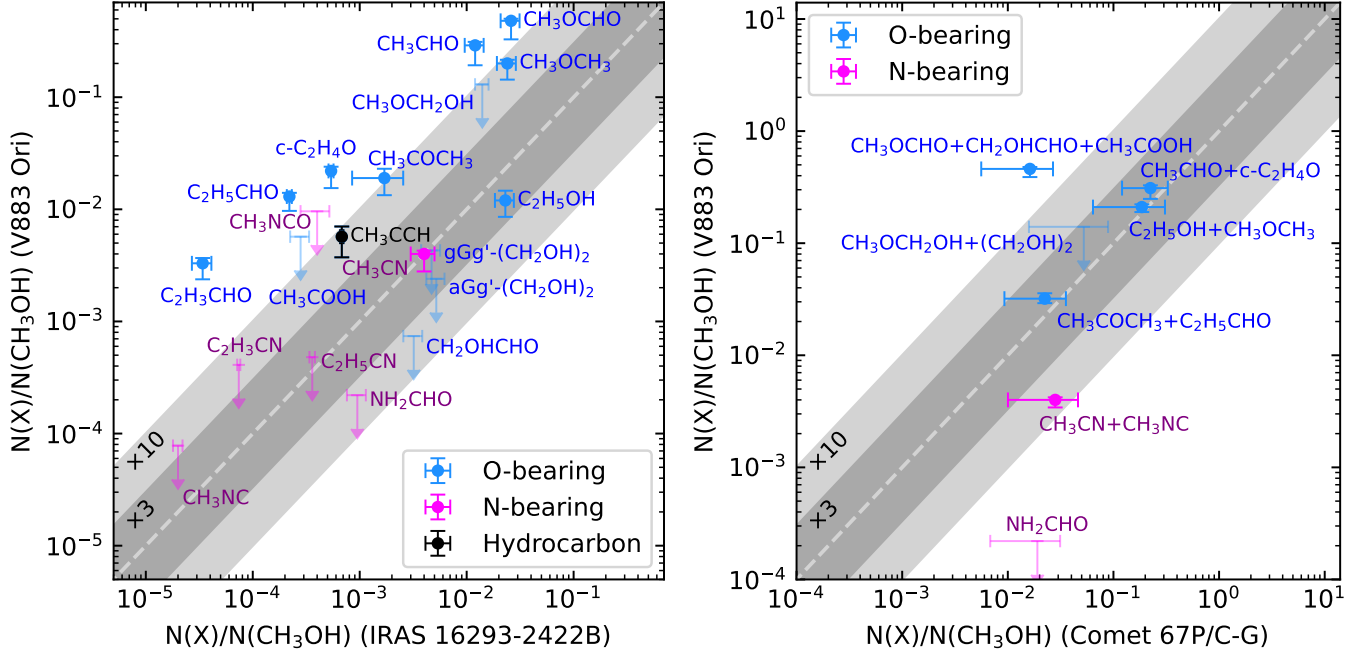


Figure 9. Comparison of the column density of COMs relative to methanol between V883 Ori & IRAS 16293-2422B (left panel, based on Table 5), and V883 Ori & Comet 67P/Churyumov-Gerasimenko (right panel). The comet data represent relative bulk compositions of species with the same mass, and are taken from [Schuhmann et al. \(2019\)](#); [Rubin et al. \(2019\)](#). For the non-detected molecules in V883 Ori, the upper limits are induced from the 3σ levels. The line representing 1:1 is indicated by a gray dashed line. The lines representing 3 times and 10 times are shown as gray solid lines with dark and light gray shaded areas, respectively.

hot corino ([Lee et al. 2023](#)), and studies for disks such as HH 212 (Class 0 disk atmosphere, [Lee et al. 2019a](#)), Oph IRS 48 (transition disk, [Brunken et al. 2022](#)), and V883 Ori (Class I/II disk including disk midplane, [Lee et al. 2019b](#); [Yamato et al. 2024](#)). We also compare with high-mass protostars: Sgr B2(N2) by ALMA/EMoCA ([Belloche et al. 2016](#); [Müller et al. 2016](#); [Bonfand et al. 2019](#); [Ordu et al. 2019](#)) and various hot cores by ALMA/CoCCoA ([Chen et al. 2023](#)) and by [Baek et al. \(2022\)](#).

Figure 10 shows the abundances of COMs relative to methanol derived from the aforementioned studies. For each study, the column density of methanol that emits optically thick lines was obtained in the following manners. $\text{CH}_3^{18}\text{OH}$ was used for PILS and CoCCoA. CALYPSO and PEACHES surveys, the study of IRS 48, the hot cores ([Baek et al. 2022](#)), and V883 Ori (from [Yamato et al. 2024](#) and this work) directly derived the column densities of methanol using its main isotopologue. ALMASOP survey, the study of V883 Ori (from [Lee et al. 2019b](#)), HOPS 373SW and HH 212 took the values calculated from $60 \times ^{13}\text{CH}_3\text{OH}$. In fact, the study of ALMASOP and HH 212 used $50 \times ^{13}\text{CH}_3\text{OH}$, but we multiplied their values by $60/50$ to make the comparison consistent.

First, we compare the results of the V883 Ori studies that used different ALMA Bands: Band 7 from [Lee et al. \(2019b\)](#), Band 3 from [Yamato et al. \(2024\)](#), and Band 6 from this work (stars in Figure 10), which are all corrected for the dust optical depth. The column densities of methanol in the three studies are similar as $3.2 \times 10^{18} \text{ cm}^{-2}$ ($= 60 \times ^{13}\text{CH}_3\text{OH}$), $3.9 \times 10^{18} \text{ cm}^{-2}$, $2.3 \times 10^{18} \text{ cm}^{-2}$, respectively. On the other hand, the relative column densities of CH_3CHO , CH_3OCHO , and CH_3CN derived from the Band 7 study are underestimated by about 5 to 14 times, while the Band 3 study and this work are consistent within about a factor of two. This can be attributed to the line optical depth effect, which is examined in Section 4.2, because both the Band 3 study and this work used only optically thin lines to estimate column densities.

Therefore, it is important to take into account the line optical depth effect when estimating column densities. Otherwise, there is the potential to be underestimated several times.

Figure 10 shows a large spread in abundances across about four orders of magnitude without significant systematic differences between low-mass and high-mass protostars, as previously revealed (e.g., [Baek et al. \(2022\)](#); [Chen et al. \(2023\)](#)). Although V883 Ori falls

within these ranges, it shows some distinctive trends that make it different from other sources. Abundances of CH_3CHO , CH_3OCH_3 , and CH_3OCHO in V883 Ori tend to be higher than most of the sources. The other disk source, Oph IRS 48 (Brunken et al. 2022), shows higher values than V883 Ori, although only two molecules were compared. Also, some of PEACHES samples, including outliers, show higher abundances, which may be caused by their underestimated CH_3OH column densities, as mentioned by Yang et al. (2021).

On the other hand, $\text{C}_2\text{H}_5\text{OH}$, CH_3COCH_3 , and CH_3CN in V883 Ori are less abundant (or comparable) than (to) those of other objects. Also, the upper limit of CH_2OHCHO abundance is almost the lowest. The column density ratios using the upper limits of CH_2OH -bearing COMs verify the lack of them clearly. For example, a lower limit of the ratio between two isomers of $\text{C}_2\text{H}_4\text{O}_2$, $\text{CH}_3\text{OCHO}/\text{CH}_2\text{OHCHO}$ is 647 for V883 Ori, while the average ratio of the other sources in Figure 10 is 15.9. Similarly, a lower limit of $\text{CH}_3\text{OCHO}/(\text{CH}_2\text{OH})_2$ is 72 (see Table 5). Both values are the highest when compared to the column density ratios in various star-forming regions listed in Lykke et al. (2015) and Mininni et al. (2020). Furthermore, the average column density ratio of $\text{CH}_3\text{CHO}/\text{CH}_2\text{OHCHO}$ of the sources in Figure 10 is 2.4, while the lower limit of this ratio in V883 Ori is 394.

HOPS 373SW (Lee et al. 2023), HH 212 (Lee et al. 2019a), and the sources in the ALMASOP survey (Hsu et al. 2022) are Class 0/I protostellar sources located in the Orion clouds. Thus, they could have similar initial chemical compositions. However, V883 Ori exhibits distinctive chemical features compared to these other Orion sources. In addition, the composition of COMs detected in the disk atmosphere of HH 212 is also different from the V883 Ori disk. Therefore, this may suggest that the chemistry evolved in the deeper layers of the disk, or the physical and/or dynamic environment in V883 Ori was different.

Lastly, we note that the column densities derived in this study with a fixed beam-filling factor are likely lower limits (Appendix C). We use the beam-filling factor derived from the continuum fitting, which is consistent with the value derived from the saturated CH_3OH lines. However, the emitting area of other species might be smaller than CH_3OH . Nonetheless, this would not affect our conclusions (e.g., the extremely high lower limit of $\text{CH}_3\text{OCHO}/\text{CH}_2\text{OHCHO}$ ratio in V883 Ori).

6.2. Distinct chemical characteristics of the V883 Ori disk

As mentioned above, V883 Ori is notable for lack of CH_2OH - and nitrogen-bearing COMs, although the other oxygen-bearing COMs such as CH_3CHO , CH_3OCH_3 , and CH_3OCHO are rather abundant compared to various other sources. Likewise, in this section, we discuss the implications of these phenomena.

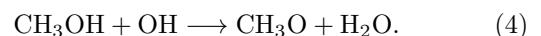
We focus on the grain-surface reactions rather than the gas-phase chemistry because the detected COMs had been trapped in the ice mantles in the quiescent phase and were sublimated by the recent outburst event. Also, the time scale of gas-phase reactions is an order of 10^4 years, which is longer than the duration of the outburst and the freeze-out time scale (Nomura et al. 2009; Lee et al. 2019b). While Taquet et al. (2016) showed that gas-phase formation of COMs could be important even in an outburst of 100 yr timescale, the key molecule in their model, ammonia (NH_3), has not been detected in V883 Ori (Tobin et al. in IAU symposium 2023). Hence, we reemphasize the fact that V883 Ori is an excellent target for studying the ice composition of a disk, which sets the initial conditions of planet formation.

6.2.1. COMs formation on water-rich ice environment

One of the important conditions in COM chemistry is the main ice component covering grain surfaces where chemical reactions occur. Although COMs have been believed to be initiated by the hydrogenation of CO on grain surfaces (Watanabe & Kouchi 2002; Garrod & Wudic Weaver 2013; Chuang et al. 2018) in the cold (< 10 K) prestellar cores, they could also form in warmer water-rich ice mantles (Bergner et al. 2017; Lamberts et al. 2017; Qasim et al. 2018; Potapov et al. 2021), where OH-radicals can be produced by photolysis of water ($\text{H}_2\text{O} + h\nu \rightarrow \text{OH} + \text{H}$).

In environments where the temperature exceeds 10 K, desorption of CO and H atoms becomes more efficient. This reduces the likelihood of high CO coverage on the ice surface, inhibiting its hydrogenation reactions. As a result, surface chemistry may become dominated by OH radicals, which are produced by water photodissociation. For example, methanol (CH_3OH) can form via reactions such as $\text{CH}_4 + \text{OH} \rightarrow \text{CH}_3 + \text{H}_2\text{O}$ and $\text{CH}_3 + \text{OH} \rightarrow \text{CH}_3\text{OH}$ (Qasim et al. 2018). Ice surface reactions driven by OH, rather than hydrogenation, could play a key role in explaining the deficiency of CH_2OH -bearing COMs in V883 Ori.

The OH-radicals can react with neighbouring methanol on the water ice surface to form CH_3O -radicals from the following reaction (Shannon et al. 2013; Ishibashi et al. 2021):



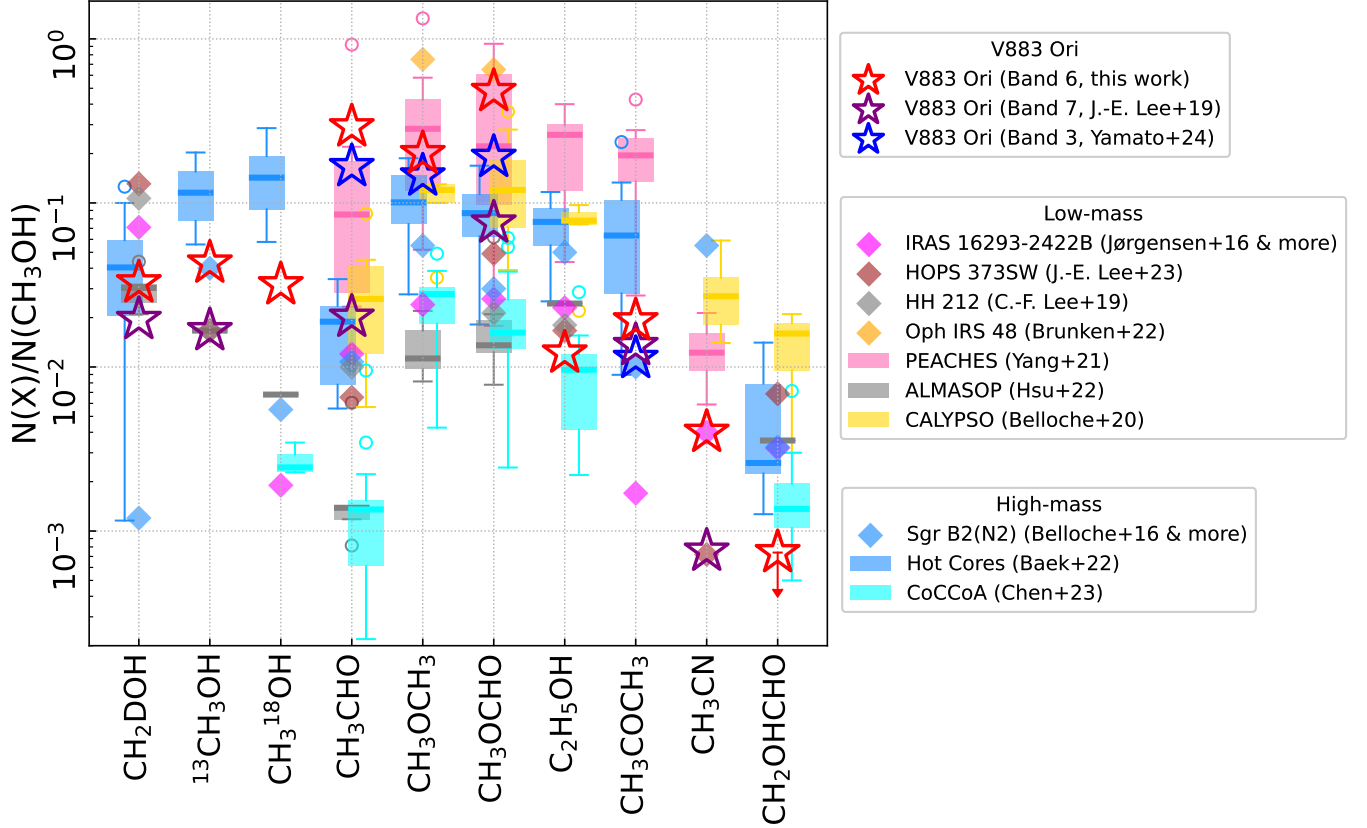
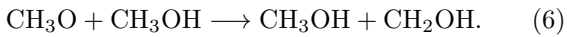


Figure 10. Column densities of COMs relative to methanol for various hot corinos/cores studies. There are three types of markers: stars for three V883 Ori studies, diamonds for five studies of a single source, and boxplots for five survey studies. The boxes of the boxplots extend across the first (Q1) to the third (Q3) quartile of the data and have a line at the median. The whiskers extend from the box to the farthest data point that is within 1.5 times the Q3–Q1 range from the box. The outliers of the distribution are shown as open circles. In legends, we separate the V883 Ori, hot corinos, and hot cores studies into three groups. For CH₂OHCHO the upper limit of V883 Ori is marked.

On the other hand, CH₂OH, which is the structurally isomeric radical of CH₃O, can be made by photodissociation of methanol (Garrod et al. 2008), and by isomerization of CH₃O (Tachikawa 1993):



However, in the OH-rich environment where water is more abundant than methanol, Reaction 4 occurs predominantly (Ishibashi et al. 2021, 2024). Furthermore, the two isomers interact with the water ice surface differently, resulting in different reactivity. For example, CH₂OH reacts with hydrogen more easily than CH₃O and is therefore consumed more efficiently (Enrique-Romero et al. 2022). As a result, the abundance ratio of CH₃O/CH₂OH in water ice would be higher compared to CO-, and thus, methanol-dominated ice (Ishibashi et al. 2021; Enrique-Romero et al. 2022; Ishibashi et al. 2024).

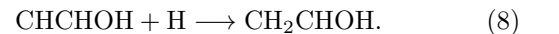
This abundance difference between the two isomeric radicals could presumably yield large amounts of CH₃O-derived products, such as methyl formate (CH₃OCHO) and dimethyl ether (CH₃OCH₃), while producing relatively small amounts of CH₂OH-derived products, such as glycolaldehyde (CH₂OHCHO) and ethylene glycol ((CH₂OH)₂).

Furthermore, laboratory studies Chuang et al. (2020) showed an important surface chemistry for acetaldehyde on the water-rich C₂H₂ ice, where CO molecules are not frozen on to the surface of dust grains, as described below.

The widely available OH-radicals can actively react with the initial C₂H₂ through reaction



Then the CHCHOH-radical combines with hydrogen, forming vinyl alcohol (CH₂CHOH),



These vinyl alcohol molecules eventually isomerize to acetaldehyde ($\text{CH}_2\text{CHOH} \longleftrightarrow \text{CH}_3\text{CHO}$) over the star-formation time scale because acetaldehyde has a lower potential energy than vinyl alcohol (Chuang et al. 2020).

The water-rich environment can be developed when the temperature is high enough to prevent CO from being frozen on grain surfaces (van Dishoeck 2014). Moreover, Kouchi et al. (2021) reported that CO can be crystallized on icy grains, with the result that the water ice mantle is not fully covered by CO. Then, CH_3OH can easily react with water molecules. The time scale of crystallization of CO on water ice becomes shorter as the grain temperature rises (Kouchi et al. 2021).

Based on the D/H ratio of COMs detected in ALMA Band 3, Yamato et al. (2024) suggested that COMs form on the lukewarm ($\sim 30\text{-}50$ K) grain surfaces within its disk. The D/H ratio of molecules is an important indicator of the formation temperature of those molecules (Lee & Bergin 2015). In addition, van 't Hoff et al. (2018a); van't Hoff et al. (2020) suggested that the young protostellar disks tend to be warmer than the more evolved Class II disks, which may prevent CO freeze-out onto the dust surface. Therefore, these previous studies of COMs in disks consistently support the hypothesis that the COMs in the disk around V883 Ori formed in a water-rich, lukewarm grain environment.

An interesting phenomenon may provide insight into the distinct chemical environment of V883 Ori; the $\text{H}_2\text{O}/\text{CH}_3\text{OH}$ ratio (~ 13) is about an order of magnitude lower compared to IRAS 16293-2422 (330) and Comet 67P (476) (Drozdovskaya et al. 2019). The water column density was calculated from our estimated HDO column density ($6.68 \times 10^{16} \text{ cm}^{-2}$) and the disk-averaged HDO: H_2O ratio (2.26×10^{-3}) reported by Tobin et al. (2023). The high methanol abundance relative to water may provide constraints on the chemical processes occurring in the water-rich ice environment inferred for V883 Ori. Further exploration with chemical models will be essential for a more comprehensive understanding.

6.2.2. Nitrogen-bearing COMs

Another intriguing characteristic of COMs in V883 Ori is that nitrogen-bearing COMs, except for methyl cyanide (CH_3CN), are missing (Lee et al. (2019b); Yamato et al. (2024), and this work). The only detected nitrogen-bearing COM, CH_3CN , also has a low abundance compared to other sources (see Figure 10). For the oxygen-bearing COMs, only CH_2OH -bearing species are exclusively absent, while the nitrogen-bearing COMs are missing regardless of their containing radicals. For example, NH_2CHO (NH_2 -radical), CH_3NCO (NCO -radical), $\text{C}_2\text{H}_3\text{CN}$ (CN -radical), and $\text{C}_2\text{H}_5\text{CN}$ (CN -

radical), which were detected in IRAS 16293-2422B, were not detected in V883 Ori (Table 3).

This distinct chemical phenomenon suggests that nitrogen-bearing COMs detected in hot cores and hot corinos (Mininni et al. 2023; Taniguchi et al. 2023) may have formed via gas-phase chemistry following the sublimation of ammonia (NH_3) from ice mantles into the gas phase. Given that the time scale for the gas-phase chemistry of COMs (Nomura et al. 2009) is much longer than the time scale of the outburst event, the duration following the burst in V883 Ori may not be sufficient for the formation of nitrogen-bearing COMs.

Before the burst, ammonia, present in a water-rich ice mixture (e.g., $\text{H}_2\text{O}:\text{CO}:\text{NH}_3$), is expected to have easily formed NH_2CHO (Chuang et al. 2022) and sublimated during the burst. However, in V883 Ori, NH_2CHO showed only a low upper limit of abundance, suggesting that ammonia did not participate in the formation of NH_2CHO . This nondetection of NH_2CHO may imply that most nitrogen is sequestered in refractory components, such as ammonium salts within the disk, and that nitrogen-bearing COMs rarely form in this environment (Boogert et al. 2015; Öberg et al. 2023; Yamato et al. 2024).

This hypothesis aligns with observations of comets, which are partly composed of ice from the disk midplane and also show a depletion of nitrogen-bearing molecules. Altwegg et al. (2020a) suggested that nitrogen in Comet 67P/C-G is primarily trapped as ammonium salts (e.g., NH_4^+Cl^- , NH_4^+CN^- , $\text{NH}_4^+\text{OCN}^-$, $\text{NH}_4^+\text{HCOO}^-$, and $\text{NH}_4^+\text{CH}_3\text{COO}^-$). More recently, NH_4^+SH^- was identified as the most abundant ammonium salt (Altwegg et al. 2022).

Ammonium salts have higher sublimation temperatures than COMs, meaning that their base (ammonia) or acids (e.g., HCl , HNCO , HCN , H_2S) may exist closer to the inner disk regions. However, the high dust opacity toward the central region complicates testing this hypothesis. To better explore the nitrogen reservoir in V883 Ori, observations at wavelengths longer than those used in ALMA Band 3 (Yamato et al. 2024) will be essential. Additionally, since V883 Ori is the only disk source where various COMs have been detected in the disk midplane, further observations of additional disk sources are needed to confirm whether disk midplanes are consistently barren of nitrogen-bearing COMs.

6.3. Carbon isotope ratios of COMs

Isotope fractionation occurs under specific conditions, such as cold regions and/or intense UV radiation (e.g., Lyons et al. 2018; Nomura et al. 2023). Isotope ratio between ^{12}C - and ^{13}C - bearing isotopologues can be frac-

tionated through the isotope-selective photodissociation of CO (Visser et al. 2009) or the isotope exchange reactions such as $^{13}\text{C}^+ + \text{CO} \rightleftharpoons \text{C}^+ + ^{13}\text{CO} + 35\text{K}$ (Langer et al. 1984; Woods & Willacy 2009; Loison et al. 2020). In this section, we derive the carbon isotope ratio of COMs based on the column density estimates in Section 5.2.

Figure 11 shows $^{12}\text{C}/^{13}\text{C}$ ratios that are calculated from every species whose carbon isotopologues are detected in V883 Ori. The ratios are calculated by dividing pure column densities without any statistical correction. The blue circles indicate the ratios using only optically thin lines ($\tau_{\nu,\text{line}} < 0.7$), while the brown circles denote ratios calculated using all lines. The average isotopic ratio derived from only optically thin lines is 3.4 times higher than that derived from all lines because many lines of the ^{12}C -bearing isotopologues are optically thick, and thus, their column densities could be underestimated, as seen in the Section 4.2.

As a result, in V883 Ori, the COMs have the $^{12}\text{C}/^{13}\text{C}$ ratio of 24.4 on average (from minimum 9.6 to maximum 38.5), which is distinct from the local ISM values (~ 50 – 70 , Kahane et al. 2018; Langer & Penzias 1993; Milam et al. 2005) and the value derived from methanol in the Comet 67P/C-G (91, Altwegg et al. 2020b). However, this low ratio is consistent with the value ~ 20 – 30 presented by Yamato et al. (2024). It is also similar to the results of the PILS survey, with 17 for dimethyl ether and 27 for glycolaldehyde (Jørgensen et al. 2016, 2018). HOPS 373SW also shows a low carbon isotopic ratio if $\text{CH}_3\text{OH } \nu_{12}=2$ is employed for the calculation of a methanol abundance (Lee et al. 2023). Furthermore, $^{12}\text{CH}_3\text{OH}/^{13}\text{CH}_3\text{OH}$ isotope ratios derived from several hot cores range from 5 to 20 (Baek et al. 2022). Therefore, the carbon isotope fractionation of COMs occurs in general during the star formation process, although its origins have not been thoroughly investigated yet (Jørgensen et al. 2016, 2018).

7. SUMMARY

Utilizing our unbiased spectral survey of a low-mass, eruptive young star V883 Ori in ALMA Band 6 over the frequency coverage of ~ 55 GHz (220.7 to 274.9 GHz), we analyzed freshly sublimated Complex Organic Molecules (COMs) in the Keplerian disk around V883 Ori, which is believed to have erupted ~ 130 years ago and has not had time to modify the initial ice chemical composition. Throughout the analysis, we used the disk-averaged spectra, which were extracted using the first principal component (PC1) filtering method. This is the first study that fully investigated freshly sublimated COMs in a disk of a young stellar object using unbiased

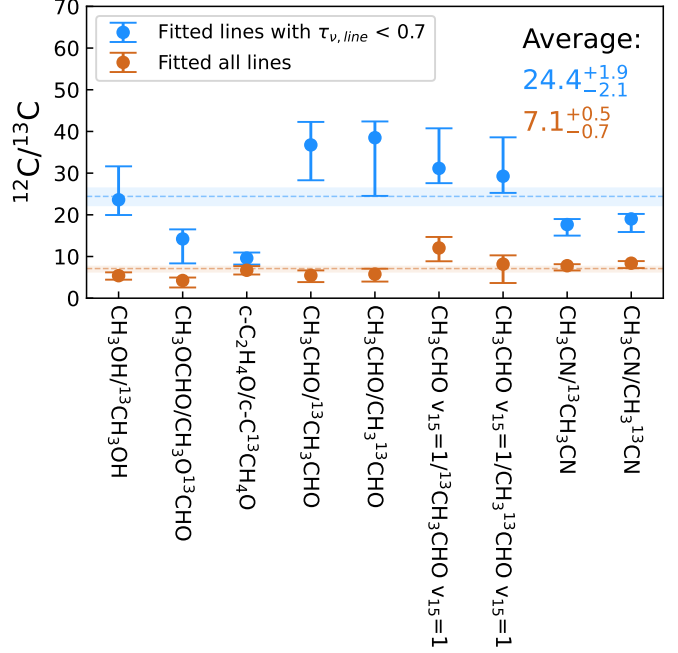


Figure 11. $^{12}\text{C}/^{13}\text{C}$ isotopic ratios. The column density results using isolated lines of $\tau_{\nu,\text{line}}$ smaller than 0.7 (Table 1) and using isolated lines of all $\tau_{\nu,\text{line}}$ are plotted respectively. The dashed lines represent the average $^{12}\text{C}/^{13}\text{C}$ values and the shaded areas show the 1σ error range for the average values.

line survey data. The main findings of this study are summarized as follows:

1. We examined every possible species in the spectral range ($\sim 1,500$ species) through a systematic method and robustly discovered 23 COMs, including isotopologues, by identifying about 3,700 molecular emission lines ($\sim 80\%$ of detected lines). These are mostly oxygen-bearing COMs. On the other hand, CH_2OH - and nitrogen-bearing COMs, except for methyl cyanide, are missing in V883 Ori.
2. The disk-averaged spectra contain numerous optically thick molecular lines. Therefore, an iterative LTE line fitting method was used to properly derive the column densities of detected COMs, adopting only optically thin lines. Through this method, we showed that the column density of some molecules (e.g., methyl formate) could be underestimated by a factor of a few unless only optically thin lines were adopted for the line-fitting process. Thanks to our robust line identification over the abnormally wide frequency range, we could collect a sufficient number of optically thin, isolated lines for each species.

3. Compared to various Class 0/I hot corinos, V883 Ori shows extremely high $\text{CH}_3\text{OCHO}:\text{CH}_2\text{OHCHO}$, $\text{CH}_3\text{CHO}:\text{CH}_2\text{OHCHO}$, and $\text{CH}_3\text{OCHO}:(\text{CH}_2\text{OH})_2$ ratios. The total budget of carbon and oxygen within complex molecules is concentrated on the detected COMs rather than spreading out over more diverse species.
4. Compared to another disk source (Oph IRS 48) and a Solar System comet (67P/C-G), the abundances of the detected COMs seem comparable.
5. The COMs in the V883 Ori disk may have formed in a water-rich ice environment. The OH-radicals, which are widely available in the water-rich ice, can cause significant differences in abundance between CH_3O - and CH_2OH -radicals. They can also be used efficiently for OH-radical addition chemical reactions, resulting in the deficiency of CH_2OH -bearing COMs in V883 Ori.
6. All nitrogen-bearing COMs are missing in V883 Ori with the exception of CH_3CN , which has a low abundance compared to other COM-rich sources. According to previous observations of the Solar System comet (67P/C-G), nitrogen might be trapped as ammonium salt in the dust grains.
7. The average $^{12}\text{C}/^{13}\text{C}$ ratio estimated from various COMs detected in V883 Ori is 24.4, which is comparable to the ratios calculated from the other hot corino/core sources but lower by $\sim 2-4$ times when compared to the ratios in the Comet 67P/C-G and the local ISM.

8. ACKNOWLEDGEMENTS

We greatly appreciate the thorough and constructive review by the anonymous referees. This work was supported by the New Faculty Startup Fund from Seoul National University and the NRF grant funded by the Korean government (MSIT) (grant numbers 2021R1A2C1011718 and RS-2024-00416859). JHJ was supported by the National Research Foundation of Korea (NRF) grant (NRF- 2019R1A2C2010885). GB was supported by Basic Science Research Program through the National Research Foundation of Korea (NRF) funded by the Ministry of Education (RS-2023-00247790). Y.A. acknowledges support by MEXT/JSPS Grants-in-Aid for Scientific Research (KAKENHI) Grant Numbers JP20H05847 and JP24K00674, and NAOJ ALMA Scientific Research Grant code 2019-13B. DJ is supported by NRC Canada and by an NSERC Discovery Grant. LC acknowledges financial support from ANID FONDECYT grant #1211656.

This paper makes use of the following ALMA data: ADS/JAO.ALMA#2019.1.00377.S. ALMA is a partnership of ESO (representing its member states), NSF (USA) and NINS (Japan), together with NRC (Canada), MOST and ASIAA (Taiwan), and KASI (Republic of Korea), in cooperation with the Republic of Chile. The Joint ALMA Observatory is operated by ESO, AUI/NRAO and NAOJ.

- *Facility:* ALMA
- *Software:* Numpy (Harris et al. 2020), Scipy (Virtanen et al. 2020a), Astropy (Astropy Collaboration et al. 2013, 2018, 2022), Pandas (Virtanen et al. 2020b), Matplotlib (Hunter 2007), XCLASS (Möller et al. 2017)

REFERENCES

- Agúndez, M., Marcelino, N., Tercero, B., et al. 2021, *A&A*, 649, L4, doi: [10.1051/0004-6361/202140978](https://doi.org/10.1051/0004-6361/202140978)
- Aikawa, Y., Okuzumi, S., & Pontoppidan, K. 2022, arXiv e-prints, arXiv:2212.14529, doi: [10.48550/arXiv.2212.14529](https://doi.org/10.48550/arXiv.2212.14529)
- Altwegg, K., Balsiger, H., Hänni, N., et al. 2020a, *Nature Astronomy*, 4, 533, doi: [10.1038/s41550-019-0991-9](https://doi.org/10.1038/s41550-019-0991-9)
- Altwegg, K., Balsiger, H., Combi, M., et al. 2020b, *MNRAS*, 498, 5855, doi: [10.1093/mnras/staa2701](https://doi.org/10.1093/mnras/staa2701)
- Altwegg, K., Combi, M., Fuselier, S. A., et al. 2022, *MNRAS*, 516, 3900, doi: [10.1093/mnras/stac2440](https://doi.org/10.1093/mnras/stac2440)
- Astropy Collaboration, Robitaille, T. P., Tollerud, E. J., et al. 2013, *A&A*, 558, A33, doi: [10.1051/0004-6361/201322068](https://doi.org/10.1051/0004-6361/201322068)
- Astropy Collaboration, Price-Whelan, A. M., Sipőcz, B. M., et al. 2018, *AJ*, 156, 123, doi: [10.3847/1538-3881/aabc4f](https://doi.org/10.3847/1538-3881/aabc4f)
- Astropy Collaboration, Price-Whelan, A. M., Lim, P. L., et al. 2022, *ApJ*, 935, 167, doi: [10.3847/1538-4357/ac7c74](https://doi.org/10.3847/1538-4357/ac7c74)
- Baek, G., Lee, J.-E., Hirota, T., Kim, K.-T., & Kim, M. K. 2022, *ApJ*, 939, 84, doi: [10.3847/1538-4357/ac81d3](https://doi.org/10.3847/1538-4357/ac81d3)
- Belloche, A., Müller, H. S. P., Garrod, R. T., & Menten, K. M. 2016, *A&A*, 587, A91, doi: [10.1051/0004-6361/201527268](https://doi.org/10.1051/0004-6361/201527268)

- Belloche, A., Maury, A. J., Maret, S., et al. 2020, *A&A*, 635, A198, doi: [10.1051/0004-6361/201937352](https://doi.org/10.1051/0004-6361/201937352)
- Bergner, J. B., Öberg, K. I., & Rajappan, M. 2017, *ApJ*, 845, 29, doi: [10.3847/1538-4357/aa7d09](https://doi.org/10.3847/1538-4357/aa7d09)
- Bonfand, M., Belloche, A., Garrod, R. T., et al. 2019, *A&A*, 628, A27, doi: [10.1051/0004-6361/201935523](https://doi.org/10.1051/0004-6361/201935523)
- Boogert, A. C. A., Gerakines, P. A., & Whittet, D. C. B. 2015, *ARA&A*, 53, 541, doi: [10.1146/annurev-astro-082214-122348](https://doi.org/10.1146/annurev-astro-082214-122348)
- Brunken, N. G. C., Booth, A. S., Leemker, M., et al. 2022, *A&A*, 659, A29, doi: [10.1051/0004-6361/202142981](https://doi.org/10.1051/0004-6361/202142981)
- Calcutt, H., Jørgensen, J. K., Müller, H. S. P., et al. 2018a, *A&A*, 616, A90, doi: [10.1051/0004-6361/201732289](https://doi.org/10.1051/0004-6361/201732289)
- Calcutt, H., Fiechter, M. R., Willis, E. R., et al. 2018b, *A&A*, 617, A95, doi: [10.1051/0004-6361/201833140](https://doi.org/10.1051/0004-6361/201833140)
- Calcutt, H., Willis, E. R., Jørgensen, J. K., et al. 2019, *A&A*, 631, A137, doi: [10.1051/0004-6361/201936323](https://doi.org/10.1051/0004-6361/201936323)
- Ceccarelli, C., Codella, C., Balucani, N., et al. 2023, in *Astronomical Society of the Pacific Conference Series*, Vol. 534, *Protostars and Planets VII*, ed. S. Inutsuka, Y. Aikawa, T. Muto, K. Tomida, & M. Tamura, 379
- Chen, Y., van Gelder, M. L., Nazari, P., et al. 2023, *A&A*, 678, A137, doi: [10.1051/0004-6361/202346491](https://doi.org/10.1051/0004-6361/202346491)
- Chuang, K. J., Fedoseev, G., Qasim, D., et al. 2018, *ApJ*, 853, 102, doi: [10.3847/1538-4357/aaa24e](https://doi.org/10.3847/1538-4357/aaa24e)
- Chuang, K. J., Jäger, C., Krasnokutski, S. A., Fulvio, D., & Henning, T. 2022, *ApJ*, 933, 107, doi: [10.3847/1538-4357/ac7320](https://doi.org/10.3847/1538-4357/ac7320)
- Chuang, K. J., Fedoseev, G., Qasim, D., et al. 2020, *A&A*, 635, A199, doi: [10.1051/0004-6361/201937302](https://doi.org/10.1051/0004-6361/201937302)
- Cieza, L. A., Casassus, S., Tobin, J., et al. 2016, *Nature*, 535, 258, doi: [10.1038/nature18612](https://doi.org/10.1038/nature18612)
- Cieza, L. A., Ruíz-Rodríguez, D., Perez, S., et al. 2018, *MNRAS*, 474, 4347, doi: [10.1093/mnras/stx3059](https://doi.org/10.1093/mnras/stx3059)
- Coutens, A., Jørgensen, J. K., van der Wiel, M. H. D., et al. 2016, *A&A*, 590, L6, doi: [10.1051/0004-6361/201628612](https://doi.org/10.1051/0004-6361/201628612)
- Drozdovskaya, M. N., Coudert, L. H., Margulès, L., et al. 2022, *A&A*, 659, A69, doi: [10.1051/0004-6361/202142863](https://doi.org/10.1051/0004-6361/202142863)
- Drozdovskaya, M. N., van Dishoeck, E. F., Rubin, M., Jørgensen, J. K., & Altwegg, K. 2019, *MNRAS*, 490, 50, doi: [10.1093/mnras/stz2430](https://doi.org/10.1093/mnras/stz2430)
- Drozdovskaya, M. N., van Dishoeck, E. F., Jørgensen, J. K., et al. 2018, *MNRAS*, 476, 4949, doi: [10.1093/mnras/sty462](https://doi.org/10.1093/mnras/sty462)
- Dzib, S. A., Ortiz-León, G. N., Hernández-Gómez, A., et al. 2018, *A&A*, 614, A20, doi: [10.1051/0004-6361/201732093](https://doi.org/10.1051/0004-6361/201732093)
- Enrique-Romero, J., Rimola, A., Ceccarelli, C., et al. 2022, *ApJS*, 259, 39, doi: [10.3847/1538-4365/ac480e](https://doi.org/10.3847/1538-4365/ac480e)
- Ferrer Asensio, J., Spezzano, S., Coudert, L. H., et al. 2023, *A&A*, 670, A177, doi: [10.1051/0004-6361/202245442](https://doi.org/10.1051/0004-6361/202245442)
- Furlan, E., Fischer, W. J., Ali, B., et al. 2016, *ApJS*, 224, 5, doi: [10.3847/0067-0049/224/1/5](https://doi.org/10.3847/0067-0049/224/1/5)
- Garrod, R. T., & Widicus Weaver, S. L. 2013, *Chemical Reviews*, 113, 8939, doi: [10.1021/cr400147g](https://doi.org/10.1021/cr400147g)
- Garrod, R. T., Widicus Weaver, S. L., & Herbst, E. 2008, *ApJ*, 682, 283, doi: [10.1086/588035](https://doi.org/10.1086/588035)
- Goldsmith, P. F., & Langer, W. D. 1999, *ApJ*, 517, 209, doi: [10.1086/307195](https://doi.org/10.1086/307195)
- Harris, C. R., Millman, K. J., van der Walt, S. J., et al. 2020, *Nature*, 585, 357, doi: [10.1038/s41586-020-2649-2](https://doi.org/10.1038/s41586-020-2649-2)
- Herbst, E., & van Dishoeck, E. F. 2009, *ARA&A*, 47, 427, doi: [10.1146/annurev-astro-082708-101654](https://doi.org/10.1146/annurev-astro-082708-101654)
- Hollis, J. M., Vogel, S. N., Snyder, L. E., Jewell, P. R., & Lovas, F. J. 2001, *ApJL*, 554, L81, doi: [10.1086/320930](https://doi.org/10.1086/320930)
- Hsu, S.-Y., Liu, S.-Y., Liu, T., et al. 2022, *ApJ*, 927, 218, doi: [10.3847/1538-4357/ac49e0](https://doi.org/10.3847/1538-4357/ac49e0)
- Hunter, J. D. 2007, *Computing in Science and Engineering*, 9, 90, doi: [10.1109/MCSE.2007.55](https://doi.org/10.1109/MCSE.2007.55)
- Ilyushin, V. V., Müller, H. S. P., Jørgensen, J. K., et al. 2022, *A&A*, 658, A127, doi: [10.1051/0004-6361/202142326](https://doi.org/10.1051/0004-6361/202142326)
- . 2023, *A&A*, 677, A49, doi: [10.1051/0004-6361/202347105](https://doi.org/10.1051/0004-6361/202347105)
- Ishibashi, A., Hidaka, H., Oba, Y., Kouchi, A., & Watanabe, N. 2021, *ApJL*, 921, L13, doi: [10.3847/2041-8213/ac3005](https://doi.org/10.3847/2041-8213/ac3005)
- Ishibashi, A., Hidaka, H., Sameera, W. M. C., Oba, Y., & Watanabe, N. 2024, *ApJ*, 960, 90, doi: [10.3847/1538-4357/acfb82](https://doi.org/10.3847/1538-4357/acfb82)
- Jiménez-Serra, I., Rodríguez-Almeida, L. F., Martín-Pintado, J., et al. 2022, *A&A*, 663, A181, doi: [10.1051/0004-6361/202142699](https://doi.org/10.1051/0004-6361/202142699)
- Jørgensen, J. K., Belloche, A., & Garrod, R. T. 2020, *ARA&A*, 58, 727, doi: [10.1146/annurev-astro-032620-021927](https://doi.org/10.1146/annurev-astro-032620-021927)
- Jørgensen, J. K., Bourke, T. L., Nguyen Luong, Q., & Takakuwa, S. 2011, *A&A*, 534, A100, doi: [10.1051/0004-6361/201117139](https://doi.org/10.1051/0004-6361/201117139)
- Jørgensen, J. K., van der Wiel, M. H. D., Coutens, A., et al. 2016, *A&A*, 595, A117, doi: [10.1051/0004-6361/201628648](https://doi.org/10.1051/0004-6361/201628648)
- Jørgensen, J. K., Müller, H. S. P., Calcutt, H., et al. 2018, *A&A*, 620, A170, doi: [10.1051/0004-6361/201731667](https://doi.org/10.1051/0004-6361/201731667)
- Kahane, C., Jaber Al-Edhari, A., Ceccarelli, C., et al. 2018, *ApJ*, 852, 130, doi: [10.3847/1538-4357/aa9e88](https://doi.org/10.3847/1538-4357/aa9e88)
- Kouchi, A., Tsuge, M., Hama, T., et al. 2021, *MNRAS*, 505, 1530, doi: [10.1093/mnras/stab1173](https://doi.org/10.1093/mnras/stab1173)
- Lamberts, T., Fedoseev, G., Kästner, J., Ioppolo, S., & Linnartz, H. 2017, *A&A*, 599, A132, doi: [10.1051/0004-6361/201629845](https://doi.org/10.1051/0004-6361/201629845)

- Langer, W. D., Graedel, T. E., Frerking, M. A., & Armentrout, P. B. 1984, *ApJ*, 277, 581, doi: [10.1086/161730](https://doi.org/10.1086/161730)
- Langer, W. D., & Penzias, A. A. 1993, *ApJ*, 408, 539, doi: [10.1086/172611](https://doi.org/10.1086/172611)
- Lee, C.-F., Codella, C., Li, Z.-Y., & Liu, S.-Y. 2019a, *ApJ*, 876, 63, doi: [10.3847/1538-4357/ab15db](https://doi.org/10.3847/1538-4357/ab15db)
- Lee, C.-F., Li, Z.-Y., Ho, P. T. P., et al. 2017, *ApJ*, 843, 27, doi: [10.3847/1538-4357/aa7757](https://doi.org/10.3847/1538-4357/aa7757)
- Lee, J.-E., & Bergin, E. A. 2015, *ApJ*, 799, 104, doi: [10.1088/0004-637X/799/1/104](https://doi.org/10.1088/0004-637X/799/1/104)
- Lee, J.-E., Lee, S., Baek, G., et al. 2019b, *Nature Astronomy*, 3, 314, doi: [10.1038/s41550-018-0680-0](https://doi.org/10.1038/s41550-018-0680-0)
- Lee, J.-E., Baek, G., Lee, S., et al. 2023, *ApJ*, 956, 43, doi: [10.3847/1538-4357/ace34b](https://doi.org/10.3847/1538-4357/ace34b)
- Lee, J.-E., Kim, C.-H., Lee, S., et al. 2024, *ApJ*, 966, 119, doi: [10.3847/1538-4357/ad3106](https://doi.org/10.3847/1538-4357/ad3106)
- Ligterink, N. F. W., Terwisscha van Scheltinga, J., Taquet, V., et al. 2018a, *MNRAS*, 480, 3628, doi: [10.1093/mnras/sty2066](https://doi.org/10.1093/mnras/sty2066)
- Ligterink, N. F. W., Coutens, A., Kofman, V., et al. 2017, *MNRAS*, 469, 2219, doi: [10.1093/mnras/stx890](https://doi.org/10.1093/mnras/stx890)
- Ligterink, N. F. W., Calcutt, H., Coutens, A., et al. 2018b, *A&A*, 619, A28, doi: [10.1051/0004-6361/201731980](https://doi.org/10.1051/0004-6361/201731980)
- Loison, J.-C., Wakelam, V., Gratier, P., & Hickson, K. M. 2020, *MNRAS*, 498, 4663, doi: [10.1093/mnras/staa2700](https://doi.org/10.1093/mnras/staa2700)
- Lombardo, N. A., Nixon, C. A., Greathouse, T. K., et al. 2019, *ApJL*, 881, L33, doi: [10.3847/2041-8213/ab3860](https://doi.org/10.3847/2041-8213/ab3860)
- Lykke, J. M., Favre, C., Bergin, E. A., & Jørgensen, J. K. 2015, *A&A*, 582, A64, doi: [10.1051/0004-6361/201526220](https://doi.org/10.1051/0004-6361/201526220)
- Lykke, J. M., Coutens, A., Jørgensen, J. K., et al. 2017, *A&A*, 597, A53, doi: [10.1051/0004-6361/201629180](https://doi.org/10.1051/0004-6361/201629180)
- Lyons, J. R., Gharib-Nezhad, E., & Ayres, T. R. 2018, *Nature Communications*, 9, 908, doi: [10.1038/s41467-018-03093-3](https://doi.org/10.1038/s41467-018-03093-3)
- Manigand, S., Calcutt, H., Jørgensen, J. K., et al. 2019, *A&A*, 623, A69, doi: [10.1051/0004-6361/201832844](https://doi.org/10.1051/0004-6361/201832844)
- Manigand, S., Jørgensen, J. K., Calcutt, H., et al. 2020, *A&A*, 635, A48, doi: [10.1051/0004-6361/201936299](https://doi.org/10.1051/0004-6361/201936299)
- Manigand, S., Coutens, A., Loison, J. C., et al. 2021, *A&A*, 645, A53, doi: [10.1051/0004-6361/202038113](https://doi.org/10.1051/0004-6361/202038113)
- McGuire, B. A. 2022, *ApJS*, 259, 30, doi: [10.3847/1538-4365/ac2a48](https://doi.org/10.3847/1538-4365/ac2a48)
- McGuire, B. A., Carroll, P. B., Loomis, R. A., et al. 2016, *Science*, 352, 1449, doi: [10.1126/science.aae0328](https://doi.org/10.1126/science.aae0328)
- Milam, S. N., Savage, C., Brewster, M. A., Ziurys, L. M., & Wyckoff, S. 2005, *ApJ*, 634, 1126, doi: [10.1086/497123](https://doi.org/10.1086/497123)
- Mininni, C., Beltrán, M. T., Rivilla, V. M., et al. 2020, *A&A*, 644, A84, doi: [10.1051/0004-6361/202038966](https://doi.org/10.1051/0004-6361/202038966)
- Mininni, C., Beltrán, M. T., Colzi, L., et al. 2023, *A&A*, 677, A15, doi: [10.1051/0004-6361/202245277](https://doi.org/10.1051/0004-6361/202245277)
- Möller, T., Bernst, I., Panoglou, D., et al. 2013, *A&A*, 549, A21, doi: [10.1051/0004-6361/201220063](https://doi.org/10.1051/0004-6361/201220063)
- Möller, T., Endres, C., & Schilke, P. 2017, *A&A*, 598, A7, doi: [10.1051/0004-6361/201527203](https://doi.org/10.1051/0004-6361/201527203)
- Müller, H. S. P., Jørgensen, J. K., Guillemin, J.-C., Lewen, F., & Schlemmer, S. 2023, *MNRAS*, 518, 185, doi: [10.1093/mnras/stac2525](https://doi.org/10.1093/mnras/stac2525)
- Müller, H. S. P., Schlöder, F., Stutzki, J., & Winnewisser, G. 2005, *Journal of Molecular Structure*, 742, 215, doi: [10.1016/j.molstruc.2005.01.027](https://doi.org/10.1016/j.molstruc.2005.01.027)
- Müller, H. S. P., Thorwirth, S., Roth, D. A., & Winnewisser, G. 2001, *A&A*, 370, L49, doi: [10.1051/0004-6361:20010367](https://doi.org/10.1051/0004-6361:20010367)
- Müller, H. S. P., Belloche, A., Xu, L.-H., et al. 2016, *A&A*, 587, A92, doi: [10.1051/0004-6361/201527470](https://doi.org/10.1051/0004-6361/201527470)
- Nomura, H., Aikawa, Y., Nakagawa, Y., & Millar, T. J. 2009, *A&A*, 495, 183, doi: [10.1051/0004-6361:200810206](https://doi.org/10.1051/0004-6361:200810206)
- Nomura, H., Furuya, K., Cordiner, M. A., et al. 2023, in *Astronomical Society of the Pacific Conference Series*, Vol. 534, *Protostars and Planets VII*, ed. S. Inutsuka, Y. Aikawa, T. Muto, K. Tomida, & M. Tamura, 1075
- Öberg, K. I., Bottinelli, S., Jørgensen, J. K., & van Dishoeck, E. F. 2010, *ApJ*, 716, 825, doi: [10.1088/0004-637X/716/1/825](https://doi.org/10.1088/0004-637X/716/1/825)
- Öberg, K. I., Facchini, S., & Anderson, D. E. 2023, *ARA&A*, 61, 287, doi: [10.1146/annurev-astro-022823-040820](https://doi.org/10.1146/annurev-astro-022823-040820)
- Ohno, Y., Oyama, T., Tamanai, A., et al. 2022, *ApJ*, 932, 101, doi: [10.3847/1538-4357/ac6b9e](https://doi.org/10.3847/1538-4357/ac6b9e)
- Ordu, M. H., Zingsheim, O., Belloche, A., et al. 2019, *A&A*, 629, A72, doi: [10.1051/0004-6361/201935887](https://doi.org/10.1051/0004-6361/201935887)
- Oyama, T., Ohno, Y., Tamanai, A., et al. 2023, *ApJ*, 957, 4, doi: [10.3847/1538-4357/acf320](https://doi.org/10.3847/1538-4357/acf320)
- Pickett, H. M., Poynter, R. L., Cohen, E. A., et al. 1998, *JQSRT*, 60, 883, doi: [10.1016/S0022-4073\(98\)00091-0](https://doi.org/10.1016/S0022-4073(98)00091-0)
- Potapov, A., Krasnokutski, S. A., Jäger, C., & Henning, T. 2021, *ApJ*, 920, 111, doi: [10.3847/1538-4357/ac1a70](https://doi.org/10.3847/1538-4357/ac1a70)
- Qasim, D., Chuang, K. J., Fedoseev, G., et al. 2018, *A&A*, 612, A83, doi: [10.1051/0004-6361/201732355](https://doi.org/10.1051/0004-6361/201732355)
- Rubin, M., Altwegg, K., Balsiger, H., et al. 2019, *MNRAS*, 489, 594, doi: [10.1093/mnras/stz2086](https://doi.org/10.1093/mnras/stz2086)
- Sánchez-Monge, Á., Schilke, P., Ginsburg, A., Cesaroni, R., & Schmiedeke, A. 2018, *A&A*, 609, A101, doi: [10.1051/0004-6361/201730425](https://doi.org/10.1051/0004-6361/201730425)
- Sandell, G., & Weintraub, D. A. 2001, *ApJS*, 134, 115, doi: [10.1086/320360](https://doi.org/10.1086/320360)

- Schuhmann, M., Altwegg, K., Balsiger, H., et al. 2019, ACS Earth and Space Chemistry, 3, 1854, doi: [10.1021/acsearthspacechem.9b00094](https://doi.org/10.1021/acsearthspacechem.9b00094)
- Scibelli, S., & Shirley, Y. 2020, ApJ, 891, 73, doi: [10.3847/1538-4357/ab7375](https://doi.org/10.3847/1538-4357/ab7375)
- Shannon, R. J., Blitz, M. A., Goddard, A., & Heard, D. E. 2013, Nature Chemistry, 5, 745, doi: [10.1038/nchem.1692](https://doi.org/10.1038/nchem.1692)
- Strom, K. M., & Strom, S. E. 1993, ApJL, 412, L63, doi: [10.1086/186941](https://doi.org/10.1086/186941)
- Tachikawa, H. 1993, Chemical Physics Letters, 212, 27, doi: [10.1016/0009-2614\(93\)87102-9](https://doi.org/10.1016/0009-2614(93)87102-9)
- Taniguchi, K., Majumdar, L., Caselli, P., et al. 2023, ApJS, 267, 4, doi: [10.3847/1538-4365/acd110](https://doi.org/10.3847/1538-4365/acd110)
- Taquet, V., Wirström, E. S., & Charnley, S. B. 2016, ApJ, 821, 46, doi: [10.3847/0004-637X/821/1/46](https://doi.org/10.3847/0004-637X/821/1/46)
- Tobin, J. J., van't Hoff, M. L. R., Leemker, M., et al. 2023, Nature, 615, 227, doi: [10.1038/s41586-022-05676-z](https://doi.org/10.1038/s41586-022-05676-z)
- Turner, B. E., & Apponi, A. J. 2001, ApJL, 561, L207, doi: [10.1086/324762](https://doi.org/10.1086/324762)
- van Dishoeck, E. F. 2014, Faraday Discussions, 168, 9, doi: [10.1039/C4FD00140K](https://doi.org/10.1039/C4FD00140K)
- van 't Hoff, M. L. R., Tobin, J. J., Harsono, D., & van Dishoeck, E. F. 2018a, A&A, 615, A83, doi: [10.1051/0004-6361/201732313](https://doi.org/10.1051/0004-6361/201732313)
- van 't Hoff, M. L. R., Tobin, J. J., Trapman, L., et al. 2018b, ApJL, 864, L23, doi: [10.3847/2041-8213/aadb8a](https://doi.org/10.3847/2041-8213/aadb8a)
- van't Hoff, M. L. R., Harsono, D., Tobin, J. J., et al. 2020, ApJ, 901, 166, doi: [10.3847/1538-4357/abb1a2](https://doi.org/10.3847/1538-4357/abb1a2)
- Virtanen, P., Gommers, R., Oliphant, T. E., et al. 2020a, Nature Methods, 17, 261, doi: [10.1038/s41592-019-0686-2](https://doi.org/10.1038/s41592-019-0686-2)
- . 2020b, Nature Methods, 17, 261, doi: [10.1038/s41592-019-0686-2](https://doi.org/10.1038/s41592-019-0686-2)
- Visser, R., van Dishoeck, E. F., & Black, J. H. 2009, A&A, 503, 323, doi: [10.1051/0004-6361/200912129](https://doi.org/10.1051/0004-6361/200912129)
- Watanabe, N., & Kouchi, A. 2002, ApJL, 571, L173, doi: [10.1086/341412](https://doi.org/10.1086/341412)
- Woods, P. M., & Willacy, K. 2009, ApJ, 693, 1360, doi: [10.1088/0004-637X/693/2/1360](https://doi.org/10.1088/0004-637X/693/2/1360)
- Yamato, Y., Notsu, S., Aikawa, Y., et al. 2024, AJ, 167, 66, doi: [10.3847/1538-3881/ad11d9](https://doi.org/10.3847/1538-3881/ad11d9)
- Yang, Y.-L., Sakai, N., Zhang, Y., et al. 2021, ApJ, 910, 20, doi: [10.3847/1538-4357/abdf6](https://doi.org/10.3847/1538-4357/abdf6)
- Yun, H.-S., & Lee, J.-E. 2023, ApJ, 958, 113, doi: [10.3847/1538-4357/acfa6a](https://doi.org/10.3847/1538-4357/acfa6a)
- Zakharenko, O., Lewen, F., Ilyushin, V. V., et al. 2019, A&A, 621, A114, doi: [10.1051/0004-6361/201834472](https://doi.org/10.1051/0004-6361/201834472)

APPENDIX

A. ROTATION DIAGRAM ANALYSIS OF COMS

To derive the column densities of COMs, we applied iterative LTE line fitting in the main paper. For comparisons, we also adopted rotation diagrams, the most commonly used LTE analysis of molecular excitation, and here, we present the results. We used the same spectra as used for line fitting analysis, i.e., the PC1-filtered spectra corrected for dust attenuation, adopting the same beam-filling factor of 0.384.

A.1. Method

Assuming all lines are optically thin, the column density and the rotation temperature of a molecular species can be inferred using the equation below (Goldsmith & Langer 1999);

$$\ln\left(\frac{N_i}{g_i}\right) = \ln\left(\frac{N}{Q}\right) - \frac{E_i}{kT_{\text{rot}}}. \quad (\text{A1})$$

The following equation can calculate the upper-level column density (N_i) relevant to each line;

$$N_i = \frac{8\pi k\nu^2}{hc^3 A_{ij}} \int T_a dv. \quad (\text{A2})$$

Here, the g_i is the degeneracy and E_i is the energy of the upper level. Q is the partition function, which depends on the rotation temperature (T_{rot}). A_{ij} is the Einstein A coefficient and ν is the frequency of the emission line. This spectroscopic information can be obtained from CDMS and JPL molecular databases queried through Splatologue¹.

From the line identification result (Section 5.1), we selected isolated lines using the criterion of three times the channel width. Each line was fitted with a Gaussian profile to get the integrated intensity. For each molecule, the lines with large line widths, probably due to blending with other lines that are currently unidentified, are removed from the rotation diagram analysis because they tend to have bad fitting results. Only the lines of the low 80% in the linewidth distribution were used.

The example plots for the rotation diagrams are shown in Figure 12. The rotation diagram shows two representative types. For molecules whose lines are optically thin, such as $^{13}\text{CH}_3\text{OH}$ on the left panel of Fig-

ure 12, the linear fit works reasonably. However, for some COMs such as CH_3OCHO (middle, right panel), the lines are divided into two groups on the rotation diagram, resulting in an undesirable fit. The two groups have two distinct A_{ij} values. Lines with relatively higher A_{ij} show smaller column densities per degeneracy than those with relatively lower A_{ij} because they have higher optical depths (middle panel). Thus, we excluded the group with high A_{ij} and linear fitted to lines with low A_{ij} , resulting in a higher column density by a few factors (right panel).

A.2. Results of rotation diagram analysis

The molecular information could not be found for some molecules, such as $\text{C}_2\text{H}_3\text{CHO}$, so we did not fit their rotation diagrams. Molecules with less than 3 emission lines were also excluded. Finally, we reasonably fitted the rotation diagrams of 13 species.

The resulting column densities obtained from the rotation diagrams are listed in Table 4. We used the column density of $^{13}\text{CH}_3\text{OH}$ to calculate the abundances relative to CH_3OH of each molecule. The ratio between $^{13}\text{CH}_3\text{OH}$ and CH_3OH was assumed as 1:24.4, as derived from iterative LTE line fitting results in Section 6.3.

As described in Section A.1, we calculated the rotation temperatures and column densities using only lines with small A_{ij} for molecules with some of their molecular lines are attenuated. After fitting the rotation diagram, we checked if the lines with large A_{ij} are truly optically thick using XCLASS, with which we can calculate the line optical depths adopting the parameters derived from the rotation diagrams. As a result, there is a positive relation between the A_{ij} coefficient and the optical depth of the line. Therefore, using only small A_{ij} is almost equivalent to excluding lines with high optical depths.

Lastly, in Figure 13 we compared the column densities with the results from the iterative LTE line fitting. As described in the main paper, the temperature is fixed as 120 K in the line fitting method, although both the column density and rotation temperature are free parameters in rotation diagrams. The difference between the two methods has a scatter of about 0.28 dex, with a very little offset of 0.03 dex. Therefore, considering the column density range spans approximately four orders of magnitude, both methods can be regarded as consistent.

¹ <https://splatalogue.online/>

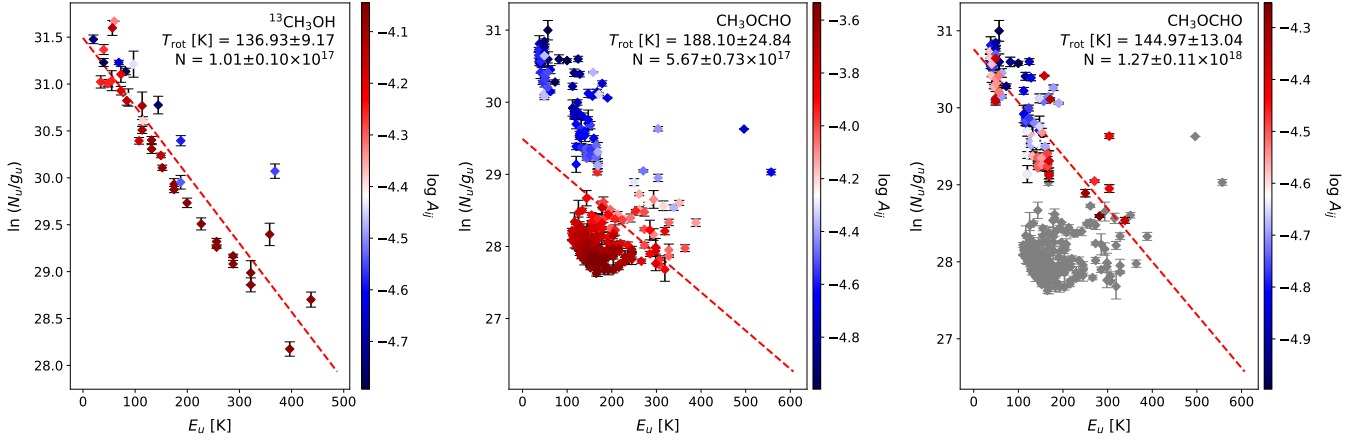


Figure 12. Example rotation diagrams for optically thin ($^{13}\text{CH}_3\text{OH}$, left panel) and thick (CH_3OCHO , center and right panels) molecules. On the right panel, the gray data points are lines with relatively high A_{ij} , and those with color are lines with relatively low A_{ij} . The red dashed line on the right panel is the result of a linear fit using only lines with low A_{ij} (colored points), while the gray dashed line shows the result when we use all lines (gray + colored points). This gray dashed line corresponds to the red dashed line in the middle panel, which shows the fitting to all data points.

Table 4. Rotation temperatures and column densities derived from rotation diagrams.

Species	T_{rot} (K)	N (cm^{-2})	$N(X)/N(\text{CH}_3\text{OH})$	Species	T_{rot} (K)	N (cm^{-2})	$N(X)/N(\text{CH}_3\text{OH})$
$\text{CH}_3\text{OH}^\dagger$	168.1(18.9)	$1.06(0.16) \times 10^{18}$	-	$\text{C}_2\text{H}_5\text{OH}$	207.7(105)	$8.84(3.32) \times 10^{16}$	3.6×10^{-2}
$\text{CH}_3\text{OH } v_{12}=1$	137.0(15.7)	$1.58(0.63) \times 10^{18}$	-	$s\text{-C}_2\text{H}_5\text{CHO}$	125.9(25.8)	$5.70(1.51) \times 10^{16}$	2.3×10^{-2}
$^{13}\text{CH}_3\text{OH}$	136.9(9.17)	$1.01(0.10) \times 10^{17}$	4.1×10^{-2}	CH_3CCH	93.6(25.0)	$9.64(3.27) \times 10^{15}$	3.9×10^{-3}
$\text{CH}_3 \text{ } ^{18}\text{OH}$	165.1(49.0)	$2.69(0.62) \times 10^{16}$	1.1×10^{-2}	CH_3OCH_3	169.6(14.2)	$9.94(0.94) \times 10^{17}$	4.0×10^{-1}
$\text{CH}_3\text{OCHO}^\dagger$	145.0(13.0)	$1.27(0.11) \times 10^{18}$	5.2×10^{-1}	CH_3CN	343.0(102)	$1.35(0.15) \times 10^{16}$	5.5×10^{-3}
$c\text{-C}_2\text{H}_4\text{O}^\dagger$	105.2(13.6)	$1.11(0.39) \times 10^{17}$	4.5×10^{-2}	$^{13}\text{CH}_3\text{CN}$	179.0(127)	$6.29(3.27) \times 10^{14}$	2.6×10^{-4}
$\text{CH}_3\text{CHO}^\dagger$	134.9(12.3)	$3.98(0.33) \times 10^{17}$	1.6×10^{-1}				

† Used lines with low Einstein-A coefficient (low optical depth).

A.3. Rotation temperature for column density estimation

Since Table 4 shows that the rotation diagrams result in higher temperatures than 120 K for some molecules, we investigated two higher rotation temperatures of 200 K and 300 K in the iterative line fitting process. For the investigation, we used different beam-filling factors (0.230, 0.154) to prevent optically thick lines from being calculated as optically thin due to the increased temperature and to keep the level of the saturated lines divided by the beam-filling factor similar to the rotation temperature. The χ^2 value was used to find the best-fit temperature for observed spectra.

For the 200 K model, the χ^2 for most species are found to be larger than those calculated at 120 K, while, for the 300 K case, all species show much larger χ^2 . The

models with higher temperatures populate high-energy transition lines, which were not detected in the observed spectra.

There are five molecular species which fit better with 200K: $\text{CH}_3\text{OCHO } v_{18}=1$, $\text{CH}_3\text{CHO } v_{15}=2$, CH_3CN , $\text{CH}_3\text{CN } v_{8}=1$, and $\text{C}_2\text{H}_5\text{OH}$. These are mostly the vibrationally excited species that were previously found to have different column densities from the ground state species when 120 K was adopted (Section 5.2). The column densities of these species increase slightly (e.g., from $6.9 \times 10^{17} \text{ cm}^{-2}$ to $8.9 \times 10^{17} \text{ cm}^{-2}$ for $\text{CH}_3\text{OCHO } v_{18}=1$; from $9.2 \times 10^{15} \text{ cm}^{-2}$ to $1.1 \times 10^{16} \text{ cm}^{-2}$ for CH_3CN), except for $\text{CH}_3\text{CN } v_{8}=1$. In fact, the column density of $\text{CH}_3\text{CN } v_{8}=1$ reduces to $1.1 \times 10^{16} \text{ cm}^{-2}$ from $2.3 \times 10^{16} \text{ cm}^{-2}$. In general, the column densities of the ground state and excited state species, which show some difference at the fixed excitation temperature of 120 K

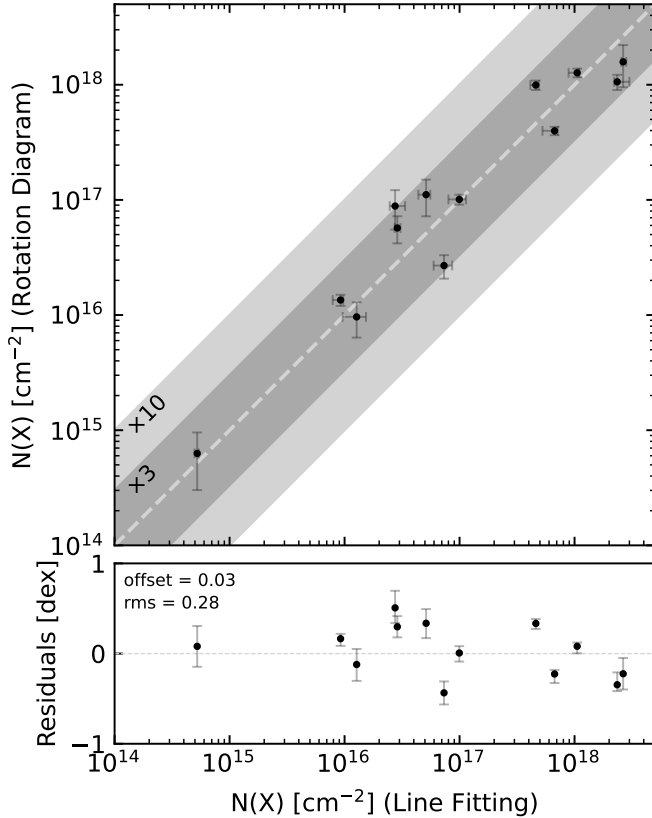


Figure 13. Comparison of column densities derived from the iterative LTE line fitting (Table 1) and from the rotation diagrams (Table 4). The 1:1 reference line is depicted as a gray dashed line. Additionally, the gray solid lines, accompanied by dark and light gray shaded regions, represent three times and ten times the reference value.

in Section 5.2, become more consistent when 200 K is adopted for the excited species.

Although the spectra of several molecules in excited vibrational states are fitted better with a higher temperature of 200 K as presented above, we opt to use a fixed temperature of 120 K to fit all molecular spectra since we extracted spectra over the entire disk and the average dust temperature over the disk is 120 K (Lee et al. 2019b). Above all, the spectra of most species are best fitted by 120 K. In addition, even for the five species mentioned above, the column densities fitted with 120 K and 200 K differ only by less than a factor of 2. As a result, our conclusion is not affected significantly by our choice of rotation temperature.

A.4. Spatial distribution of COMs

While we estimated single column density and rotation temperature per molecule using the averaged spectra extracted from the PC1-filtering method, the same procedure can be easily applied in each pixel to map the

physical parameters using the rotation diagram fitting if the lines are strong enough over multiple pixels. However, the line fitting analysis on pixel-by-pixel requires much more computational time.

From the original 200×200 pixels map with a pixel size of $0.02''$, a smaller map of 15×15 pixels with the 4×4 binning was made to reduce noise and focus on the central region with COMs emission. In this map, the pixel size is comparable with the beam size. The source has a disk rotation, which has to be corrected to identify each emission line before constructing the rotation diagram. For the velocity correction, we used the same isolated, strong lines as used for the PCA analysis (Yun & Lee 2023).

The column density and rotation temperature maps of $^{13}\text{CH}_3\text{OH}$ and CH_3CN are plotted in Figure 14. The maps for $^{13}\text{CH}_3\text{OH}$ show a consistent rotation temperature of ~ 120 K throughout the map. The column density distribution of $^{13}\text{CH}_3\text{OH}$ shows no clear asymmetry. On the other hand, the column density and rotation temperature of CH_3CN are higher in the northern part. The temperature is much higher than 150 K in most pixels, and it is even higher than 300 K in some of the northern region. This might suggest that the origin of CH_3CN could be distinct from that of other oxygen-bearing COMs. This is also consistent with the results from the averaged-spectra in Appendix A.3, where 200 K fits better the CH_3CN spectra than 120 K.

B. LINE OPTICAL DEPTH EFFECTS SEEN WITH SPECTRA

Figure 15 illustrates how significantly the spectral fitting results can differ depending on the constraint of line optical depths. The model spectra in the lower panel fit well most of the observed spectral lines, particularly the weak lines, whereas the model spectra in the upper panel fit only the few strongest lines. Likewise, the iterative fitting process only with optically thin lines enables us to identify lines that might have been missed otherwise and, thus, derive the COMs column densities more precisely.

Ideally, the model spectra fitting the weak lines must also fit the optically thick strong lines. However, the intensities of some optically thick model lines exceed those of corresponding observed lines (i.e., the lines excluded during the line fitting), as seen in the lower panel and its residual plot. This may be attributed to different beam-filling factors from what we adopted for the model spectra. Therefore, we test the effect of different beam-filling factors on the derived column densities and summarize the results in Appendix C.

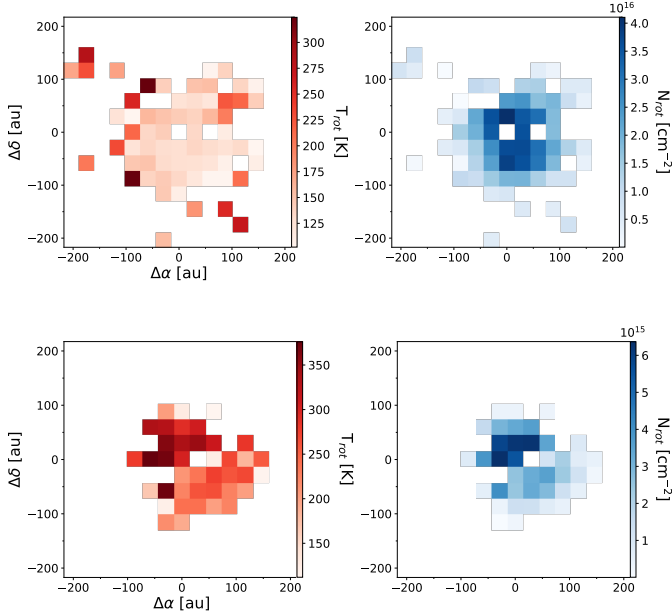


Figure 14. Rotation temperature (left) and column density (right) maps of $^{13}\text{CH}_3\text{OH}$ (top) and CH_3CN (bottom). Only pixels with fitted temperatures between 100 K and 400 K are drawn.

C. BEAM-FILLING FACTOR FOR COLUMN DENSITY ESTIMATION

Here, we investigate the beam-filling factor to fit both optically thick/saturated and thin lines for one exemplary species, methyl formate (CH_3OCHO). The beam-filling factor scales the whole spectrum, determining the maximum intensities of the saturated lines along with the rotation temperature. The rotation temperature also controls the line ratio in the LTE condition; as presented in appendix A, 120 K fits well the averaged spectra of most species.

Firstly, we test the beam-filling factor using a rotation diagram. The observational lines used in the rotation diagram analysis, where the lines are assumed to be optically thin and under the LTE condition, will be weaker than the expected line intensity by a factor of $C = \tau_{\nu,\text{line}} / (1 - e^{-\tau_{\nu,\text{line}}})$. In reality, since the optical depth for each emission line is different, this causes uncertainty in the temperature and the column density derived from the rotation diagram. This effect is clearly seen in the rotation diagram of methyl formate in Figure 12. The data points are divided into two groups because the lines with high optical depth (red symbols) have been attenuated by self-absorption.

We can calculate the line optical depth with XCLASS adopting the temperature and column density derived from the rotation diagram (Table 4) and recalculate the

intensities of each line after correcting for the optical depth effect. However, correction by the calculated optical depths did not merge the two groups into a linear line. Many lines with high A_{ij} had optical depth around $\tau \sim 3.5$, which corresponds to a factor of ~ 3.5 in the column densities in the rotation diagram. The column density must be higher than the current value ($1.27 \times 10^{18} \text{ cm}^{-2}$) by a factor of 10/6 to raise the group of optically thick lines (red symbols) and merge with the group of optically thin lines (blue symbols).

However, the higher column density also affects other lines. Here, we can play with the beam-filling factor. As mentioned above, the beam-filling factor is set to 0.384, but a value of 0.23 (0.384×0.6) resulted in a better linear fit for the rotation diagram of CH_3OCHO .

In the intensity maps of some CH_3OCHO lines (Paper I), the emission distributes along a ring structure with the outer radius of $\sim 0.2''$. The inner radius of the ring structure is $0.1''$, which is caused by the optically thick dust continuum in the inner region ($< 0.1''$) (Cieza et al. 2016). Since the spectrum was extracted from a COMs-rich region with a radius of about $0.3''$, following the definition in Möller et al. (2017), the beam-filling factor of the CH_3OCHO emission is around 1/4, similar to 0.23.

We tested line fitting by adopting the beam-filling factor of 0.23, although the beam-filling factor could vary with transitions even in a molecular species. The rotation temperature of 120 K and beam-filling factor of 0.23 match the upper bound of saturated lines of methyl formate, which is about 28 K after the dust attenuation correction. Thus, the line fitting was done with one free parameter (column density) only to isolated, optically thin lines of methyl formate. As a result, the model spectra well fitted both optically thick, saturated lines and weak lines. The obtained column density is $2.1 \times 10^{18} \text{ cm}^{-2}$, which is about 1.9 times higher than the value obtained in the line fitting method (Table 1), and 1.7 times higher than the rotation diagram method (Table 4). The optical depths of optically thick lines in this model increase to 6–7, as intended.

The emission size of most molecules is likely similar to or smaller than the size of CH_3OH emission, which is used as a standard. Therefore, the accurate beam-filling factors of less abundant molecules can increase the column densities by a factor of $\sim 2 - 3$, so the current values can be considered lower limits. However, the beam-filling factor varies with both molecules and transitions. If we perform line fitting with beam-filling factor and column density as free parameters, the parameters do not converge well.

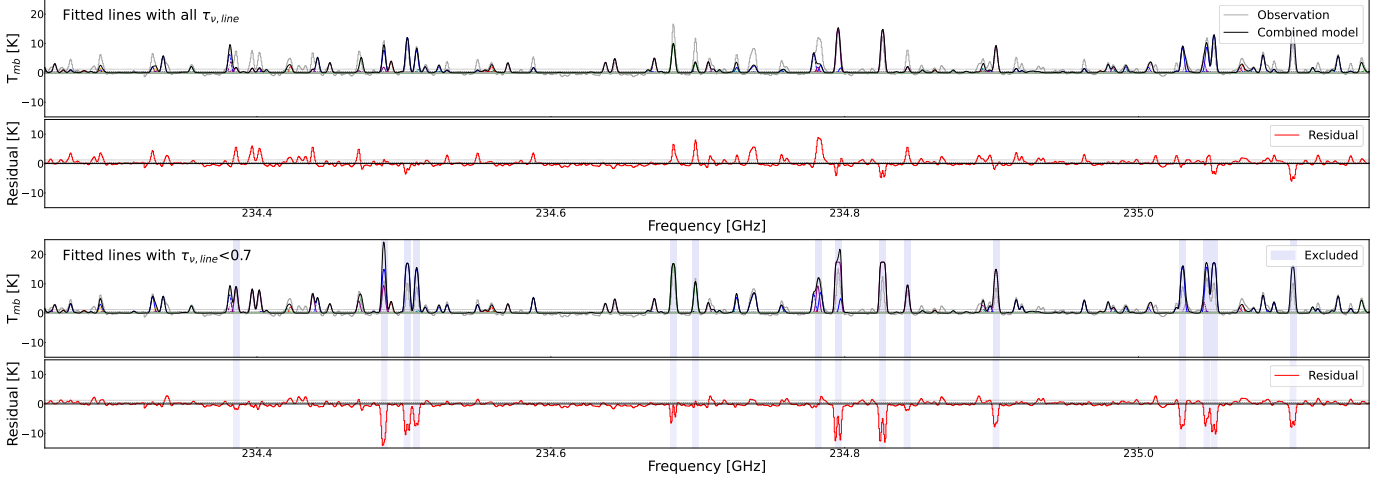


Figure 15. LTE line-fitted model spectra when using isolated molecular lines of all line optical depths (upper panel of this figure, and x-axis of Figure 6), and when using isolated lines of $\tau_{\nu, \text{line}} < 0.7$ (lower panel of this figure, and y-axis of Figure 6). Both panels show the same spectral window. Black solid lines represent the combined spectra of the model spectra for each species, and the individual model spectra are shown as various line colors and styles. The red solid lines indicate residual between the observed data and the model. The gray dashed/dotted horizontal lines represent the $1\sigma/3\sigma$ levels of the observed spectrum. Also, the blue shaded areas on the lower panel indicate lines excluded during the LTE line fitting because their modeled optical depths exceeded 0.7. This frequency region is the same as the frequency region in the lower panel of Figure 2.

Therefore, we leave this as a caveat of the current analysis but note that the column density ratios such as isotope ratios would not change significantly because

the increase of column density by a smaller beam-filling factor would not vary much from molecule to molecule.

D. COMPARISON WITH ALMA/PILS SURVEY

In this Appendix, we provide a table that was discussed in Section 6.1.1.

Table 5. Comparison of the observed COMs and their abundances in V883 Ori and IRAS 16293-2422B.

No.	Species	N (cm ⁻²)		N(X)/N(CH ₃ OH)		Reference ^a
		V883 Ori ^b	IRAS 16293-2422B	V883 Ori ^c	IRAS 16293-2422B	
Methanol						
1	CH ₃ OH	2.3×10^{18}	1.0×10^{19}	1.0	1.0	11
	CH ₃ OH $\nu_{12}=1$	2.6×10^{18}	$-^d$	$1.1 \times 10^{+0}$	-	-
	CH ₃ OH $\nu_{12}=2$	2.1×10^{18}	-	9.1×10^{-1}	-	-
2	¹³ CH ₃ OH	9.9×10^{16}	-	4.3×10^{-2}	-	1
3	CH ₂ DOH	7.5×10^{16}	7.1×10^{17}	3.3×10^{-2}	7.1×10^{-2}	11
4	CHD ₂ OH	$< 1.2 \times 10^{16}^e$	1.8×10^{17}	$< 5.2 \times 10^{-3}$	1.8×10^{-2}	19
5	CH ₃ OD	-	1.8×10^{17}	-	1.8×10^{-2}	11
6	CD ₃ OH	$< 6.2 \times 10^{15}$	3.1×10^{16}	$< 2.7 \times 10^{-3}$	3.1×10^{-3}	18
7	CD ₃ OD	-	$< 2.0 \times 10^{15}$	-	$< 2.0 \times 10^{-4}$	20
8	CH ₃ ¹⁸ OH	7.3×10^{16}	1.9×10^{16}	3.2×10^{-2}	1.9×10^{-3}	3
Methyl formate						
9	CH ₃ OCHO	1.1×10^{18}	2.6×10^{17}	4.8×10^{-1}	2.6×10^{-2}	11
	CH ₃ OCHO $\nu_{18}=1$	6.9×10^{17}	-	3.0×10^{-1}	-	-
10	CH ₃ OCDO	-	1.5×10^{16}	-	1.5×10^{-3}	11
11	CH ₂ DOCHO	-	4.8×10^{16}	-	4.8×10^{-3}	11
12	CH ₃ O ¹³ CHO	7.4×10^{16}	$< 6.3 \times 10^{15}$	3.2×10^{-2}	$< 6.3 \times 10^{-4}$	11
13	CHD ₂ OCHO	-	1.1×10^{16}	-	1.1×10^{-3}	12

Table 5 continued

Table 5 (continued)

No.	Species	N (cm ⁻²)		N(X)/N(CH ₃ OH)		Reference ^a
		V883 Ori ^b	IRAS 16293-2422B	V883 Ori ^c	IRAS 16293-2422B	
Ethanol						
14	C ₂ H ₅ OH	2.8 × 10 ¹⁶	2.3 × 10 ¹⁷	1.2 × 10 ⁻²	2.3 × 10 ⁻²	11
15	a-a-CH ₂ DCH ₂ OH	< 6.5 × 10 ¹⁵	2.7 × 10 ¹⁶	< 2.8 × 10 ⁻³	2.7 × 10 ⁻³	11
16	a-s-CH ₂ DCH ₂ OH	< 6.5 × 10 ¹⁵	1.3 × 10 ¹⁶	< 2.8 × 10 ⁻³	1.3 × 10 ⁻³	11
17	a-CH ₃ CHDOH	< 6.4 × 10 ¹⁵	2.3 × 10 ¹⁶	< 2.8 × 10 ⁻³	2.3 × 10 ⁻³	11
18	a-CH ₃ CH ₂ OD	< 6.4 × 10 ¹⁵	< 1.1 × 10 ¹⁶	< 2.8 × 10 ⁻³	< 1.1 × 10 ⁻³	11
19	a-CH ₃ ¹³ CH ₂ OH	< 6.1 × 10 ¹⁵	< 9.1 × 10 ¹⁵	< 2.7 × 10 ⁻³	< 9.1 × 10 ⁻⁴	11
20	a- ¹³ CH ₃ CH ₂ OH	< 6.2 × 10 ¹⁵	< 9.1 × 10 ¹⁵	< 2.7 × 10 ⁻³	< 9.1 × 10 ⁻⁴	11
Acetaldehyde						
21	CH ₃ CHO	6.7 × 10 ¹⁷	1.2 × 10 ¹⁷	2.9 × 10 ⁻¹	1.2 × 10 ⁻²	4
	CH ₃ CHO v ₁₅ =1	5.7 × 10 ¹⁷	–	2.5 × 10 ⁻¹	–	–
	CH ₃ CHO v ₁₅ =2	4.0 × 10 ¹⁷	–	1.7 × 10 ⁻¹	–	–
22	CH ₃ CDO	9.8 × 10 ¹⁵	7.4 × 10 ¹⁵	4.3 × 10 ⁻³	7.4 × 10 ⁻⁴	11
23	¹³ CH ₃ CHO	1.8 × 10 ¹⁶	1.8 × 10 ¹⁵	7.8 × 10 ⁻³	1.8 × 10 ⁻⁴	11
	¹³ CH ₃ CHO v ₁₅ =1	1.8 × 10 ¹⁶	–	7.8 × 10 ⁻³	–	–
24	CH ₃ ¹³ CHO	1.7 × 10 ¹⁶	1.8 × 10 ¹⁵	7.4 × 10 ⁻³	1.8 × 10 ⁻⁴	11
	CH ₃ ¹³ CHO v ₁₅ =1	2.0 × 10 ¹⁶	–	8.7 × 10 ⁻³	–	–
25	CH ₂ DCHO	2.1 × 10 ¹⁶	6.2 × 10 ¹⁵	9.1 × 10 ⁻³	6.2 × 10 ⁻⁴	16
Acetone						
26	CH ₃ COCH ₃	4.4 × 10 ¹⁶	1.7 × 10 ¹⁶	1.9 × 10 ⁻²	1.7 × 10 ⁻³	4
Ethylene glycol						
27	aGg'-(CH ₂ OH) ₂	< 5.5 × 10 ¹⁵	5.2 × 10 ¹⁶	< 2.4 × 10 ⁻³	5.2 × 10 ⁻³	3
28	gGg'-(CH ₂ OH) ₂	< 9.8 × 10 ¹⁵	4.7 × 10 ¹⁶	< 4.3 × 10 ⁻³	4.7 × 10 ⁻³	3
Dimethyl ether						
29	CH ₃ OCH ₃	4.6 × 10 ¹⁷	2.4 × 10 ¹⁷	2.0 × 10 ⁻¹	2.4 × 10 ⁻²	11
30	¹³ CH ₃ OCH ₃	–	1.4 × 10 ¹⁶	–	1.4 × 10 ⁻³	11
31	asym-CH ₂ DOCH ₃	–	4.1 × 10 ¹⁶	–	4.1 × 10 ⁻³	11
32	sym-CH ₂ DOCH ₃	–	1.2 × 10 ¹⁶	–	1.2 × 10 ⁻³	11
Glycolaldehyde						
33	CH ₂ OHCHO	< 1.7 × 10 ¹⁵	3.2 × 10 ¹⁶	< 7.4 × 10 ⁻⁴	3.2 × 10 ⁻³	3
34	CHDOHCHO	–	3.3 × 10 ¹⁵	–	3.3 × 10 ⁻⁴	3
35	CH ₂ ODCHO	–	1.5 × 10 ¹⁵	–	1.5 × 10 ⁻⁴	3
36	CH ₂ OHCDO	–	1.6 × 10 ¹⁵	–	1.6 × 10 ⁻⁴	3
37	¹³ CH ₂ OHCHO	–	1.2 × 10 ¹⁵	–	1.2 × 10 ⁻⁴	3
38	CH ₂ OH ¹³ CHO	–	1.2 × 10 ¹⁵	–	1.2 × 10 ⁻⁴	3
Acetic acid						
39	CH ₃ COOH	< 1.3 × 10 ¹⁶	2.8 × 10 ¹⁵	< 5.7 × 10 ⁻³	2.8 × 10 ⁻⁴	3
Propanal						
40	C ₂ H ₅ CHO	2.9 × 10 ¹⁶	2.2 × 10 ¹⁵	1.3 × 10 ⁻²	2.2 × 10 ⁻⁴	4
Ethylene oxide						
41	c-C ₂ H ₄ O	5.1 × 10 ¹⁶	5.4 × 10 ¹⁵	2.2 × 10 ⁻²	5.4 × 10 ⁻⁴	4
42	c-C ¹³ CH ₄ O	5.3 × 10 ¹⁵	–	2.3 × 10 ⁻³	–	–
Trans-ethyl methyl ether						
43	t-C ₂ H ₅ OCH ₃	–	1.8 × 10 ¹⁶	–	1.8 × 10 ⁻³	16
Methoxymethanol						
44	CH ₃ OCH ₂ OH	< 3.0 × 10 ¹⁷	1.4 × 10 ¹⁷	< 1.3 × 10 ⁻¹	1.4 × 10 ⁻²	16
2-Propenal						
45	C ₂ H ₃ CHO	7.7 × 10 ¹⁵	3.4 × 10 ¹⁴	3.3 × 10 ⁻³	3.4 × 10 ⁻⁵	17
Isopropyl alcohol						
46	n-C ₃ H ₇ OH	< 1.1 × 10 ¹⁶	< 3.0 × 10 ¹⁵	< 4.8 × 10 ⁻³	< 3.0 × 10 ⁻⁴	17
47	i-C ₃ H ₇ OH ^f	< 4.3 × 10 ¹⁶	< 3.0 × 10 ¹⁵	< 1.9 × 10 ⁻²	< 3.0 × 10 ⁻⁴	17
2-Propynal						

Table 5 continued

Table 5 (continued)

No.	Species	N (cm ⁻²)		N(X)/N(CH ₃ OH)		Reference ^a
		V883 Ori ^b	IRAS 16293-2422B	V883 Ori ^c	IRAS 16293-2422B	
48	HCCCHO	< 2.2 × 10 ¹⁵	< 5.0 × 10 ¹⁴	< 9.6 × 10 ⁻⁴	< 5.0 × 10 ⁻⁵	17
			Glyoxal			
49	cis-HC(O)CHO	–	< 5.0 × 10 ¹³	–	< 5.0 × 10 ⁻⁶	17
			Propyne			
50	CH ₃ CCH	1.3 × 10 ¹⁶	6.8 × 10 ¹⁵	5.7 × 10 ⁻³	6.8 × 10 ⁻⁴	15
51	CH ₃ ¹³ CCH	< 4.8 × 10 ¹⁵	< 2.4 × 10 ¹⁴	< 2.1 × 10 ⁻³	< 2.4 × 10 ⁻⁵	15
52	¹³ CH ₃ CCH	< 4.9 × 10 ¹⁵	< 2.5 × 10 ¹⁴	< 2.1 × 10 ⁻³	< 2.5 × 10 ⁻⁵	15
53	CH ₃ C ¹³ CH	< 5.0 × 10 ¹⁵	< 2.5 × 10 ¹⁴	< 2.2 × 10 ⁻³	< 2.5 × 10 ⁻⁵	15
54	CH ₃ CCD	< 5.3 × 10 ¹⁵	< 7.9 × 10 ¹⁴	< 2.3 × 10 ⁻³	< 7.9 × 10 ⁻⁵	15
55	CH ₂ DCCH	< 5.3 × 10 ¹⁵	< 2.6 × 10 ¹⁴	< 2.3 × 10 ⁻³	< 2.6 × 10 ⁻⁵	15
			Propylene			
56	C ₃ H ₆	–	4.2 × 10 ¹⁶	–	4.2 × 10 ⁻³	17
			Propane			
57	C ₃ H ₈	< 1.9 × 10 ¹⁸	< 8.0 × 10 ¹⁶	< 8.3 × 10 ⁻¹	< 8.0 × 10 ⁻³	17
			Methyl cyanide			
58	CH ₃ CN	9.2 × 10 ¹⁵	4.0 × 10 ¹⁶	4.0 × 10 ⁻³	4.0 × 10 ⁻³	7
	CH ₃ CN v ₈ =1	2.3 × 10 ¹⁶	4.0 × 10 ¹⁶	1.0 × 10 ⁻²	4.0 × 10 ⁻³	7
59	¹³ CH ₃ CN	5.2 × 10 ¹⁴	6.0 × 10 ¹⁴	2.3 × 10 ⁻⁴	6.0 × 10 ⁻⁵	7
60	CH ₃ ¹³ CN	4.9 × 10 ¹⁴	5.0 × 10 ¹⁴	2.1 × 10 ⁻⁴	5.0 × 10 ⁻⁵	7
61	CH ₃ C ¹⁵ N	< 1.9 × 10 ¹⁴	1.6 × 10 ¹⁴	< 8.3 × 10 ⁻⁵	1.6 × 10 ⁻⁵	7
62	CH ₂ DCN	1.2 × 10 ¹⁵	1.4 × 10 ¹⁵	5.2 × 10 ⁻⁴	1.4 × 10 ⁻⁴	7
63	CHD ₂ CN	< 3.2 × 10 ¹⁴	2.0 × 10 ¹⁴	< 1.4 × 10 ⁻⁴	2.0 × 10 ⁻⁵	7
			Methyl isocyanide			
64	CH ₃ NC	< 1.8 × 10 ¹⁴	2.0 × 10 ¹⁴	< 7.8 × 10 ⁻⁵	2.0 × 10 ⁻⁵	8
			Formamide			
65	NH ₂ CHO	< 5.0 × 10 ¹⁴	9.5 × 10 ¹⁵	< 2.2 × 10 ⁻⁴	9.5 × 10 ⁻⁴	2
66	NH ₂ CDO	< 5.6 × 10 ¹⁴	2.1 × 10 ¹⁴	< 2.4 × 10 ⁻⁴	2.1 × 10 ⁻⁵	2
67	cis-NHDCHO	< 5.4 × 10 ¹⁴	2.1 × 10 ¹⁴	< 2.3 × 10 ⁻⁴	2.1 × 10 ⁻⁵	2
68	trans-NHDCHO	< 5.2 × 10 ¹⁴	1.8 × 10 ¹⁴	< 2.3 × 10 ⁻⁴	1.8 × 10 ⁻⁵	2
69	NH ₂ ¹³ CHO	< 4.9 × 10 ¹⁴	1.5 × 10 ¹⁴	< 2.1 × 10 ⁻⁴	1.5 × 10 ⁻⁵	2
70	¹⁵ NH ₂ CHO	< 5.0 × 10 ¹⁴	< 1.0 × 10 ¹⁴	< 2.2 × 10 ⁻⁴	< 1.0 × 10 ⁻⁵	2
71	NH ₂ CH ¹⁸ O	< 5.2 × 10 ¹⁴	< 0.8 × 10 ¹⁴	< 2.3 × 10 ⁻⁴	< 8.0 × 10 ⁻⁶	2
			Glycine			
72	NH ₂ CH ₂ COOH	< 2.2 × 10 ¹⁶	< 9.2 × 10 ¹⁴	< 9.6 × 10 ⁻³	< 9.2 × 10 ⁻⁵	14
			Acetamide			
73	CH ₃ C(O)NH ₂	–	< 9.0 × 10 ¹⁴	–	< 9.0 × 10 ⁻⁵	10
			Methyl isocyanate			
74	CH ₃ NCO	< 2.2 × 10 ¹⁶	4.0 × 10 ¹⁵	< 9.6 × 10 ⁻³	4.0 × 10 ⁻⁴	5
75	CH ₃ CNO	< 2.9 × 10 ¹⁴	< 5.0 × 10 ¹³	< 1.3 × 10 ⁻⁴	< 5.0 × 10 ⁻⁶	5
76	CH ₃ OCN	< 1.0 × 10 ¹⁵	< 5.0 × 10 ¹⁴	< 4.3 × 10 ⁻⁴	< 5.0 × 10 ⁻⁵	5
			Methylamine			
77	CH ₃ NH ₂	< 1.3 × 10 ¹⁶	< 5.3 × 10 ¹⁴	< 5.7 × 10 ⁻³	< 5.3 × 10 ⁻⁵	9
			Vinyl cyanide			
78	C ₂ H ₃ CN	< 9.5 × 10 ¹⁴	7.4 × 10 ¹⁴	< 4.1 × 10 ⁻⁴	7.4 × 10 ⁻⁵	7
			Ethyl cyanide			
79	C ₂ H ₅ CN	< 1.1 × 10 ¹⁵	3.6 × 10 ¹⁵	< 4.8 × 10 ⁻⁴	3.6 × 10 ⁻⁴	7
			Methyl mercaptan			
80	CH ₃ SH	–	4.8 × 10 ¹⁵	–	4.8 × 10 ⁻⁴	6
81	CH ₃ SD	< 5.4 × 10 ¹⁵	< 8.8 × 10 ¹⁴	< 2.3 × 10 ⁻³	< 8.8 × 10 ⁻⁵	13

Table 5 continued

Table 5 (*continued*)

No.	Species	N (cm ⁻²)		N(X)/N(CH ₃ OH)		Reference ^a
		V883 Ori ^b	IRAS 16293-2422B	V883 Ori ^c	IRAS 16293-2422B	
References. (1) Jørgensen et al. 2011; (2) Coutens et al. 2016; (3) Jørgensen et al. 2016; (4) Lykke et al. 2017; (5) Ligterink et al. 2017; (6) Drozdovskaya et al. 2018; (7) Calcutt et al. 2018a; (8) Calcutt et al. 2018b; (9) Ligterink et al. 2018b; (10) Ligterink et al. 2018a; (11) Jørgensen et al. 2018; (12) Manigand et al. 2019; (13) Zakharenko et al. 2019; (14) Drozdovskaya et al. 2019; (15) Calcutt et al. 2019; (16) Manigand et al. 2020; (17) Manigand et al. 2021; (18) Ilyushin et al. 2022; (19) Drozdovskaya et al. 2022; (20) Ilyushin et al. 2023.						

^a References for IRAS 16293-2422B.

^b Used column densities derived using LTE line fitting method (Table 1).

^c Since only optically thin lines were used in the line fitting, we adopted the column density value for CH₃OH as it is, and then divided it directly to calculate the CH₃OH relative abundance of the other molecules.

^d The – represents that there is no information on whether this species has been detected or not.

^e 3 σ upper limits for the non-detected molecules.

^f N(g-i-C₃H₇OH) + N(a-i-C₃H₇OH)